Ultrafast magnetization dynamics describe the physics of a magnetic system on the perturbation by a strong laser pulse. This pulse excites the electrons close to the Fermi energy. It is followed by a thermalization due to a variety of scattering processes. The plenitude of these processes is of fundamental interest for solid states physics, but is not yet understood properly. In the field of ultrafast magnetization dynamics most progress was achieved by all optical measurements. However, the interpretation of all optical experiments is still under debate. In order to gain direct insight into the time evolution of the spin polarization a time and spin-resolved pump-probe experiment is applied. This allows one to measure the quenching of the spin polarization without any optical contributions. In our experiment the spin polarization of the photoexcited electrons of in situ prepared thin Fe and Co films is measured directly with a Mott-detector. The overall signal shape matches the one of the all optical measurements. Thus, with the help of our measurements it could thus be shown, that the all optical techniques indeed contain a contribution of magnetic origin.

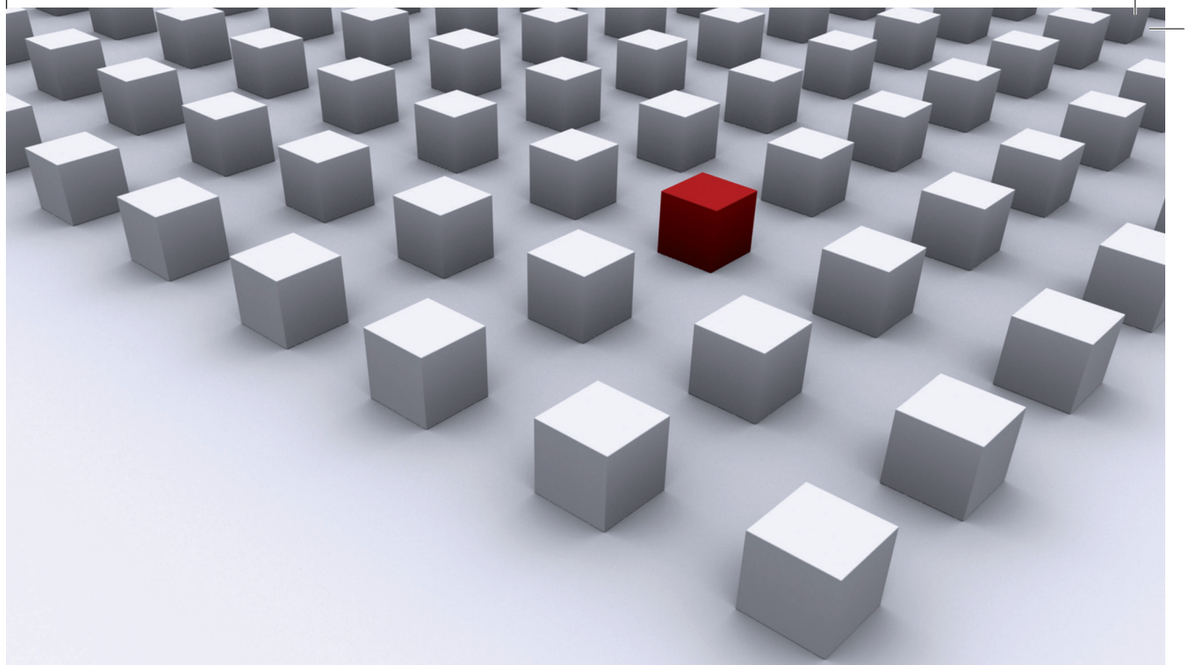

Dissertationsreihe Physik - Band 28

Alexander Weber

Ultrafast Spindynamics in Ferromagnetic Thin Films

Universitätsverlag Regensburg

a

Universitätsverlag Regensburg

ISBN 978-3-86845-089-7

gefördert von:

Alumni der physikalischen Fakultät der Universität Regensburg e.V.

Universität Regensburg

Alexander Weber

28

Dissertationsreihe Physik

Universitätsverlag Regensburg

Alexander Weber

Ultrafast Spindynamics in Ferromagnetic Thin Films

Ultrafast Spindynamics in Ferromagnetic Thin Films

Dissertation zur Erlangung des Doktorgrades der Naturwissenschaften (Dr. rer. nat.)
der Fakultät für Physik der Universität Regensburg
vorgelegt von

Alexander Weber
aus Regensburg
2010

Die Arbeit wurde von Prof. Dr. C. H. Back angeleitet.
Das Promotionsgesuch wurde am 30.06.2010 eingereicht.

Prüfungsausschuss:	Vorsitzender:	Prof. Dr. V. Braun
	1. Gutachter:	Prof. Dr. C. H. Back
	2. Gutachter:	Prof. Dr. J. Repp
	weiterer Prüfer:	Prof. Dr. C. Strunk

Dissertationsreihe der Fakultät für Physik der Universität Regensburg, Band 28

Herausgegeben vom Präsidium des Alumnivereins der Physikalischen Fakultät:
Klaus Richter, Andreas Schäfer, Werner Wegscheider, Dieter Weiss

Alexander Weber

Ultrafast Spindynamics in Ferromagnetic Thin Films

Universitätsverlag Regensburg

Bibliografische Informationen der Deutschen Bibliothek.
Die Deutsche Bibliothek verzeichnet diese Publikation
in der Deutschen Nationalbibliografie. Detailierte bibliografische Daten
sind im Internet über http://dnb.ddb.de abrufbar.

1. Auflage 2012
© 2012 Universitätsverlag, Regensburg
Leibnizstraße 13, 93055 Regensburg

Konzeption: Thomas Geiger
Umschlagentwurf: Franz Stadler, Designcooperative Nittenau eG
Layout: Alexander Weber
Druck: Docupoint, Magdeburg
ISBN: 978-3-86845-089-7

Alle Rechte vorbehalten. Ohne ausdrückliche Genehmigung des Verlags ist es nicht gestattet, dieses Buch oder Teile daraus auf fototechnischem oder elektronischem Weg zu vervielfältigen.

Weitere Informationen zum Verlagsprogramm erhalten Sie unter:
www.univerlag-regensburg.de

Ultrafast Spindynamics in Ferromagnetic Thin Films

Dissertation

zur Erlangung des Doktorgrades der Naturwissenschaften (Dr. rer. nat.)

der Naturwissenschaftlichen Fakultät II - Physik

der Universität Regensburg

vorgelegt von

Alexander Weber

aus Regensburg

2010

. . . . . .

Promotionsgesuch eingereicht am:	30.06.2010	
Tag der mündlichen Prüfung:	17.01.2012	
Die Arbeit wurde angeleitet von:	Prof. Dr. C. H. Back	
Prüfungsausschuss:	Prof. Dr. V. Braun	(Vorsitzender)
	Prof. Dr. C. H. Back	(1. Gutachter)
	Prof. Dr. J. Repp	(2. Gutachter)
	Prof. Dr. C. Strunk	(Prüfer)

"Die Natur versteht gar keinen Spaß, sie ist immer wahr, immer ernst, immer strenge; sie hat immer Recht und die Fehler und Irrtümer sind immer die des Menschen."

– Goethe

Contents

1 Introduction

In simple words: From my point of view magnetism is one of the most interesting fields of physics: Although magnets are part of every day life the underlying physics of magnetism requires the two fundamental theories of the so-called modern physics. No Newtonian approximation or any other classical concept is able to explain magnetism. The understanding of a simple magnet necessitates the theory of quantum mechanics and the special relativity theory, both theories otherwise found only on very small or very large length scales. But a simple magnet, such as the one used to pin cooking recipes to a refrigerator, is one of the few objects, which brings these theories into every day life. But it is hardly common knowledge, that heating a magnet will reduce and finally switch-off its magnetic properties, so that it would fall off the fridge. Yet this temperature dependence is of high interest for a physicist, as it is determined by the influence of the theories mentioned above. Thus, this phase transition from the ferromagnetic to the paramagnetic state was and still is a topic of great interest. The experiments presented in this thesis take the idea of heating a magnet one step further: The question asked here is how fast can the magnetization be switched off. Accordingly, the heating is not applied in such a way, that the whole system stays in an equilibrium during heating, but the *heat* is brought into the system so quickly, that it triggers all sorts of dynamics, which finally lead to an equilibrium again. But these processes are not yet understood properly. Moreover these magnetization dynamics are the fastest processes known today in the field of magnetism and are not too far from the fastest processes ever measured. If ever the maxim of *higher, faster, further* could be applied to modern research, the part of *faster*

would for sure be appropriate here.

A more elaborate description: A look into the time scales in magnetism shows a wide spectrum: from spin glass relaxation which takes minutes to hours, over domain wall motion in the range of microseconds to seconds, over magnons and spin precessional motion on a time scale of picoseconds, down to Stoner excitations and Elliott- Yafet-like spin flip scattering in the femtosecond regime. Triggering the processes on the very end of this scale with strong laser pulses opened a new topic in magnetism, the so-called ultrafast or femtosecond magnetization dynamics. In this 14 years old field, a large number of questions arose, mostly of fundamental nature, going as far as introducing a new channel of angular momentum transfer in oder to fulfill the conservation of angular momentum. Some of the major topics within the field are the thermalization of highly excited electrons, the energy and angular momentum transport to spins and phonons, and the time scales involved in these processes. These questions are of fundamental nature to solid state physics. And despite all the effort put into the topic we are still not able to understand the observed behavior properly, let alone describe them from basic principles. Moreover, the interpretation of the measured data, in some cases, is still debated. This makes the field of ultrafast magnetization dynamics so interesting.

1.1 Motivation

For most people the second question after asking the topic of my research was *and what is the application?* Having an application right at hand would of course be a strong motivation for research. But one has to wonder, whether a motivation for research by means of an application is needed, if there is still something not understood properly. Furthermore, some rather important discoveries in research took more than 100 years until they found their way into a commercial product. For instance, the magneto optic Kerr effect, discovered in 1877 [1], was not used outside research until the mini-disc player came on the market in 1991 [2]. Inversely, recent hard drive reading devices utilized the giant magneto resistance effect, which was discovered just two decades ago in 1988 [3].

So, to estimate the possible applications can be very difficult.

The processes studied in this thesis are several thousand times faster than a modern computer can perform a single calculation. The application for femtosecond magnetization dynamics is far out of my vision, but considering the rapid development in spintronics [4], the knowledge of the interplay of the microscopic processes might one day easily play an important role. Moreover, the hard drive industry is still pushing the limits of storage densities and will need to overcome the so-called superparamagnetic limit [5]. One promising approach is heat assisted magnetic recording, which takes advantage of the smaller switching field needed, if the media is heated up [6]. Indeed, the original motivation for femtosecond dynamics arose from the possibility to control magnetization on these ultrashort time scales. Today it is clear, that the understanding of the fundamental processes on very short time scales is of fundamental importance. But the little knowledge developed is still debated. Even todays standard measurement technique, the magneto optic Kerr effect is still not fully understood concerning the results it yields within these fast dynamics.

The question what really is measured in all optical experiments motivated this thesis. The title of [7], *Ultrafast Magneto-Optics in Nickel: Magnetism or Optics?*, somehow summarized the problem at that time: The all optical experiments could not completely distinguish whether the measured signal has its origin in magnetic or optic effects. Measuring directly the spin polarization provides a completely different approach with a direct insight into the time-evolution of the spin-system after excitation with a femtosecond laser-pulse.

Besides, as the experiments had to be carried out under ultra high vacuum conditions no cap layers were needed which could have had an influence on the signal. The combination of spin analysis with ultrafast dynamics was not an established method, and at the time we started the project, we did not at all know, if it would yield any signal at all; as the only time resolved spin polarization measurement published [8], showed a completely different behavior than the optical approaches and did not fit at all in the developed frame of the theoretical descriptions (see page 65 in Sec 7.2). Thus, employing this technique was

both, quite challenging and of fundamental interest for the field of ultrafast magnetism as well as for the overall field of solid states physics.

1.2 Scope of the Thesis

The goal of the project presented in this work was to investigate the time dependence of the spin polarization after the excitation with a strong laser pulse. Therefore an experimental setup for stroboscopic pump-probe experiments capable of detecting the spin polarization of photoexcited electrons was established. Additionally a new evaporation chamber was designed and built, which allowed us to do the whole sample preparation and measurement in situ. The assembly within the measurement chamber was redesigned to fulfill the special requirements of the experiment, including a pivoting sample carrier, air coils, heating, etc. The major challenge was to bring the spin analyzer, a Mott-detector, to operation. The next sticking point was the combination of the pump-probe technique with the spin analysis.

In order to comprehend the results quantitatively and to be able to compare the gained data with the literature, procedures and techniques for the focus determination, the overlap positioning etc. needed to be developed.

We managed to measure the dynamic response of the spin polarization for iron and cobalt films, each grown on a tungsten single crystal. The results are qualitatively comparable to our magneto-optic Kerr effect measurements and the measurements in literature, which mostly used the magneto-optic Kerr effect. The differences are discussed and will be explained.

This Thesis is structured as follows:

Chapter 2 gives an overview of the processes involved and the understanding we have today of ultrafast magnetization dynamics. The most basic model, the three temperature model is introduced. The chapter concludes with a convention on the names of time constants throughout the thesis.

In **Chapter 3** the theory concerning the measurements is explained. Besides the all optical methods special emphasis is put on the theory of photo emission and the operation of a Mott detector.

Chapter 4 contains a summary of the results presented in literature since 1997. The chapter aims at giving an overview of the facts, which define the actual consensus.

In **Chapter 5** the experimental setup for the spin dynamic experiments is explained.

Chapter 6 introduces the alignments necessary for the measurements. The different adjustment techniques and the measurement procedure are shown.

Chapter 7 contains the results of the spin polarization dynamics measurements. The chapter is rounded off with conclusions on the different results from the different measurement techniques.

In the **Appendix** the reader will find an introduction to the pump-probe technique, an overview on the sample preparation, some calculations on the experimental limitations, the possible angular momentum transfer by photons, an introduction to the Elliot-Yafet mechanism, and a Glossary.

2 Current Understanding

A brief description of the mechanisms involved in ultrafast magnetization dynamics from todays point of view shall be given in this chapter. An introduction of the three temperature model and a convention on the time constants will conclude this introduction to the theory.

2.1 Preface

Until now, a unifying theory considering all processes and explaining the various results in ultrafast magnetization dynamics has yet to be developed. So far, only parts of the mechanisms can be explained with separate models. Surprisingly, despite the interest the topic received because of its elementary relevance in ferromagnetism, theoretical efforts to understand the novel phenomena have been sparse. Nevertheless, several concepts could be developed from the diverse measurements. The current understanding is this: The pump beam excites enough electrons above the Fermi energy, so that the change in occupation can be observed in energy resolved photoemission experiments. The electronic system is strongly out of equilibrium, that is, the electrons do not follow a Fermi-Dirac distribution anymore. Thus, in this state no electronic temperature can be defined. This change in the electronic structure also gives rise to a change of the optical conductivity tensor, which makes the interpretation of all optical experiments so difficult. The electrons start to thermalize due to electron-electron (e-e) scattering, and after the thermalization, which takes a few to tens of femtoseconds, an elevated electronic temperature is reached and a Fermi function can be assigned again. But the electronic system is not yet in

an equilibrium with the lattice. Energy is thus transferred to the lattice due to electron-phonon (e-p) scattering. The electronic system cools down and the lattice heats up. These scattering processes involve a certain spin flip probability, claimed by Elliott and Yafet*. With the spin flips energy is transferred into the spin system and angular momentum is transfered to the lattice, resulting in a quenching of the magnetization. This is more likely to happen close to so-called hot spots, which are hybridization points of energy bands with opposite spins. At these hot spots the spin quantum number is not defined and angular momentum is transferred to the lattice faster than the spin lattice relaxation time. Once, when the rate of energy gain and loss of the spin system turns towards the energy loss, the spin system starts to relax in a first, fast process, analogue to the quenching. Angular momentum is transferred back to the spin system. The electronic system and the spin system are in equilibrium with each other, but not yet with the lattice. That is why after a few ps the magnetization follows the electronic temperature, and the M(T) curve of the static magnetization can be applied† [9]. As there is no disequilibrium between electrons and spins any more and thus on channel is closed for energy transfer, now the spin system relaxes on a slower rate with the spin lattice relaxation time. The magnetization continues to recover to its initial value in a second, slower process. Once electrons, spins and lattice are in equilibrium heat diffusion cools the probed area and the magnetization is restored completely. So, finally the whole system is in equilibrium again and the initial state is restored.

2.2 The Three Temperature Model

The first approach to understand the observed magnetization dynamics was an expansion of the so called two temperature model (2TM) to the three temperature model (3TM).

*this is currently the best description to explain the behavior, but the application of the Elliott Yafet mechanism is still debated.

†it is assumed, that the magnetization is governed by the electronic temperature and not the lattice temperature. This makes the static M(T) dependence applicable here, even though the lattice and the spin system are not in equilibrium.

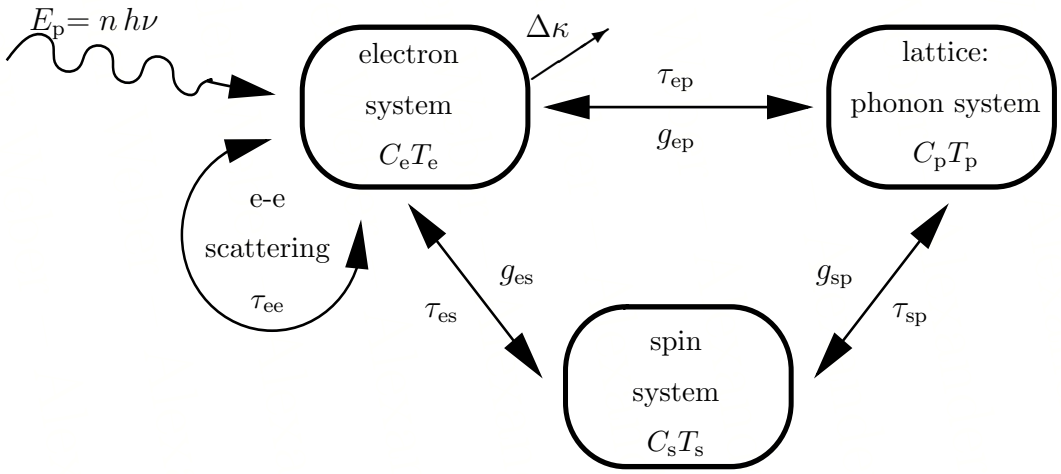

Figure 2.1 – Three Temperature Model: *The pump pulse, depicted by $h\nu$, is heating only the electron system. The lattice and spin systems are heated indirectly by the electron system. The energy transfer is described by the coupling constants g_{ij} on a time scale given by the relaxation times τ_{ij}. The heat diffusion within the electron system is indicated by $\Delta\kappa$.*

The 2TM was introduced as a rate equation model describing the energy transfer between thermal and non-thermal electron populations and a phonon heat bath, in order to understand dynamics within the electron-phonon system in non magnetic metals [10]. The 3TM, introduced in [11], is a first approach describing magnetic effects induced by strong laser pulses. In order to include the spins in the 2TM, which describes the coupling between the electron and the phonon heat bath (with temperatures T_e and T_p), a third heat bath, the spin system with temperature T_s, is introduced. T_s is defined by the dependency of the saturation magnetization M_s on the temperature: $M_s(T) \longleftrightarrow T(M_s)$. The application of a concept of such a spin temperature to the dynamics is questionable not only due to the non equilibrium within the system but also due to the absence of well-defined quasiparticle statistics for the spins [12, 13]. However it could be shown, that for times well after the initial disturbance ($t > 3$ ps), the loss in magnetization depending on the initial fluence and therefore on the temperature rise reproduces the static $M(T)$ curve [9].

Defining the heat capacities C_i, with i = e, p, and s, (for $e \hat{=}$ electrons, $p \hat{=}$ phonons,

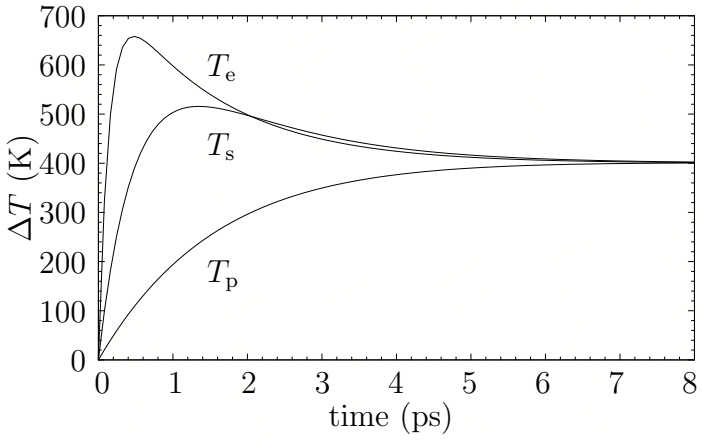

Figure 2.2 – Time dependent temperature behavior: *Illustration of the three temperatures T_e, T_s, and T_p. Spins and lattice are heated by the electron system. First the electron system equilibrates with the spin bath, later on all three systems are in thermal equilibrium again.*

and $s \hat{=}$ spins), and the coupling constants, g_{ij} (i, j = e, p, s, $i \neq j$) between the different baths, the dynamics can be written as:

$$C_e(T_e)\frac{\partial T_e}{\partial t} = \nabla\kappa\,\nabla T_e - g_{ep}(T_e - T_p) - g_{es}(T_e - T_s) + P(t); \quad (2.1)$$

$$C_p(T_p)\frac{\partial T_p}{\partial t} = g_{ep}(T_e - T_p) - g_{ps}(T_p - T_s); \quad (2.2)$$

$$C_s(T_s)\frac{\partial T_s}{\partial t} = g_{es}(T_e - T_s) + g_{ps}(T_p - T_s). \quad (2.3)$$

Eqn. (2.1) for T_e includes a heat diffusion term $\nabla\kappa\,\nabla T_e$ ($\kappa \hat{=}$ thermal conductivity within the electron bath), and the excitation $P(t)$ due to the laser pulse. The model is pictured in Fig 2.1.

The 3TM describes the energy equilibration process between the heated but already thermalized (!) electron system and the spin and the phonon systems: energy is transferred from the electron system to the spin system on a time scale given by τ_{es}, which is, in principal, dependent on all C_i's and g_{ij}'s, but dominated by g_{es}: $\tau_{es} \approx \tau_{es}(g_{es})$. The same holds for the other couplings. Of course these differential equations are by no means exhaustive but merely a first attempt to approach this field, taking into account, that energy conservation needs to be fulfilled in any case.

Before the 3TM can be applied the interaction of the heat pulse with the sample needs to be considered: The laser (pump) pulse interacts solely with the electron system. A

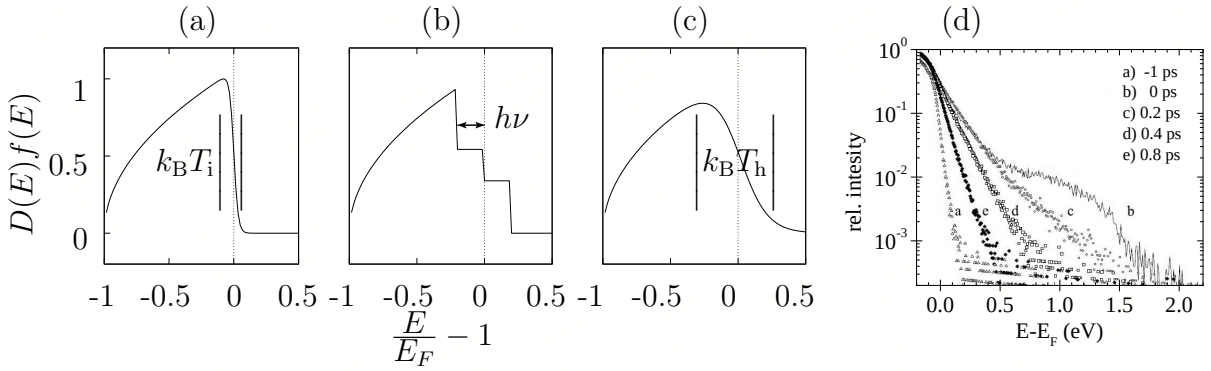

Figure 2.3 – Optical Excitation and Thermalization: *a) DOS for a free electron gas times the Fermi function for a given initial temperature T_i. b) Electron distribution directly after optical excitation with a laser pulse. c) Fermi-Dirac distribution for $T_\mathrm{h} > T_\mathrm{i}$ after the thermalization process. d) Logarithmic plot of the photoemission intensity above the Fermi energy, E_F, for various pump-probe delays measured by Rhie et al. on Ni/W(110) [14]. The missing dip below the Fermi energy is due to the finite pulse length and state refilling occurring on a fs time scale.*

non equilibrium electron distribution is induced, which scales with the photon energy (see Fig 2.3, b). Due to electron-electron (e-e) scattering the electronic system thermalizes on a time scale of $\tau_\mathrm{th} \approx 20$ to 200 fs depending on the material. Thus an elevated electron temperature is reached and the Fermi-Dirac distribution is broadened (Fig 2.3, c). This was well investigated by Rhie et al. with time and energy resolved photoemission [14] (see Fig 2.3, d).

2.3 Convention on the Time Constants throughout this Thesis

In most of the literature the measured curves were directly linked to the time constants of the different models. The time constants, used to describe the data, carry names like *demagnetization time, thermalization time, spin-lattice relaxation time* and so forth. In this thesis however the three distinct time constants, which are shown in Fig. 2.4, will simply be called τ_1, τ_2, and τ_3. The interpretation of these time constants will be treated separately. This will make the description of the results valid independent of the model and simplifies the comparison.

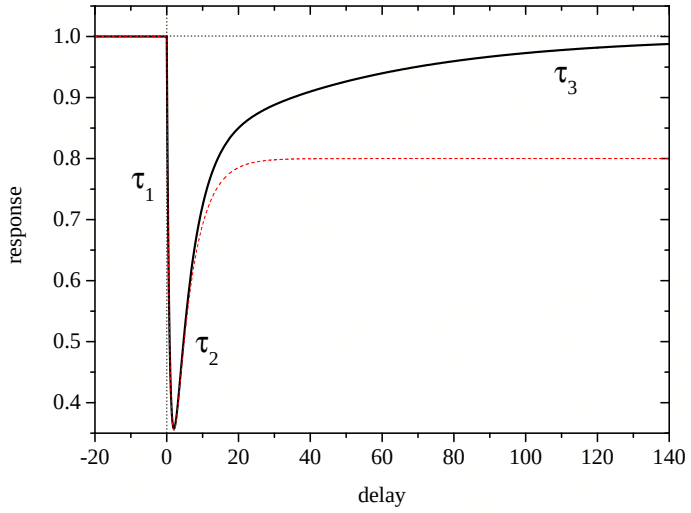

Figure 2.4 – Model Response Curve: *The graph shows a model fit function for ultrafast demagnetization. The three obvious time scales are labeled τ_1, τ_2, and τ_3. The red, dashed curved corresponds to the 2TM.*

The standard fit function used in most literature was presented by [15] as a solution for the 2TM (Part of Eqn. 2.4). It fits well for $t < 5$ ps. On longer time scales it has the disadvantage to saturate at a reduced level, in order to fit well to the first picoseconds. Therefore we expanded the function by a third exponential function $\exp(-t/\tau_3)$. With this upgrading the function fits well throughout the curves and does not change the curve within the first picoseconds:

$$1 - \left[A \left(1 - e^{\frac{-t}{\tau_1}} \right) e^{\frac{-t}{\tau_2}} + B \left(1 - e^{\frac{-t}{\tau_2}} \right) \underbrace{e^{\frac{-t}{\tau_3}}}_{t>5 \text{ ps}} \right] H(t). \tag{2.4}$$

Here $H(t)$ denotes the Heaviside step function. It is used to keep the response to zero for $t < 0$. We omitted a deconvolution of the probe pulse shape, as, in our case, the result would be changed only in the region of a percent (see App. A.4). It shall be pointed out, that Eqn. (2.4) is only used to be able to describe the results quantitatively. No direct physical interpretation is associated with it.

3 Theory behind the Experimental Techniques

This chapter will explain the theory involved with the most important measurement techniques used in ultrafast magnetization dynamics. Namely the magneto-optic Kerr effect, second harmonic generation and X-Ray circular magnetic dichroism will be introduced. Thereafter the basic concepts of photoemission and the theory of the spin analysis with a Mott detector will be explained.

3.1 All Optical Measurements

3.1.1 The Magneto-Optic Kerr Effect

The magneto-optic Kerr effect (MOKE), discovered by John Kerr in 1876/1877 [1, 16], has become an important characterization technique for magnetic films and multilayers. It was also used in magneto optical (MO) reading devices like the mini disk. A theoretical description of MOKE was first achieved 1932. Quantum mechanical approaches have been proposed by Kittel in 1951 and Argyres in 1955 [17].

MOKE is observed as a net rotation and elliptical polarization of incident linearly polarized light as it is reflected at a magnetized sample. This change in the polarization state of an incident electromagnetic wave can be described by the interaction of the electric and magnetic fields of the incident waves with the electrons in the material. In the static case the magnitude of this change in polarization is proportional to the magnetization of the sample. Right and left circularly polarized light effectively have different indices of refraction in magnetized media as they are absorbed and re-emitted

differently depending on the direction and strength of the sample's magnetization [18]. Linearly polarized light can be depicted as a combination of equal amounts of right and left circularly polarized light. The reflected light is then the sum of unequal proportions of right and left circularly polarized light; that is, the reflected light is now elliptically polarized, which can be described by $\theta = \theta_{\mathrm{K}} + i\epsilon_{\mathrm{K}}$, called the Kerr angle (θ_{K}) and the Kerr ellipticity (ϵ_{K}).

Similar effects occur in transmission. They are called the Faraday effect, if the magnetization is parallel to the plane of incidence and the Voigt effect for a perpendicular magnetization orientation [19].

All the MO effects are based on a weak dependence of the optical constants on the direction and strength of the magnetization. They can be represented by the dielectric permittivity tensor $\hat{\boldsymbol{\varepsilon}}$. For a cubic crystal it reads [20]:

$$\hat{\boldsymbol{\varepsilon}} = \varepsilon_0 \begin{bmatrix} 1 & -iQ_v m_z & iQ_v m_y \\ iQ_v m_z & 1 & -iQ_v m_x \\ -iQ_v m_y & iQ_v m_x & 1 \end{bmatrix} + \mathcal{O}(m_i^2). \tag{3.1}$$

Q_v is a material constant describing how strongly magnetism influences the sample's optical response, i.e. the magneto-optical rotation. The m_i are the components of the normalized magnetization $\vec{m} = \frac{\vec{M}}{M_s}$, where M_s is the saturation magnetization. The second term in Equation (3.1) describes effects quadratic in $\vec{m}$. Here we assume the sample to be optically isotropic in absence of a magnetization. The optical response is modified by the electron spin via the spin orbit coupling (SOC). This can be considered as a small perturbation (see Tab. 3.1) as the orbit is nearly fully quenched in 3d ferromagnets [17]. Therefore, it is sufficient to restrict oneself to effects up to the first order in M. Higher orders might contribute, but will be omitted in this description (see e.g. [21]).

In principle all situations of incident direction and polarization can be explained using Equation (3.1), the proper boundary condition and Maxwell's equations [20]. However this is not practicable in most cases. Special situations with high symmetry can be explained by using simple, classical arguments based on the Lorentz force acting on the

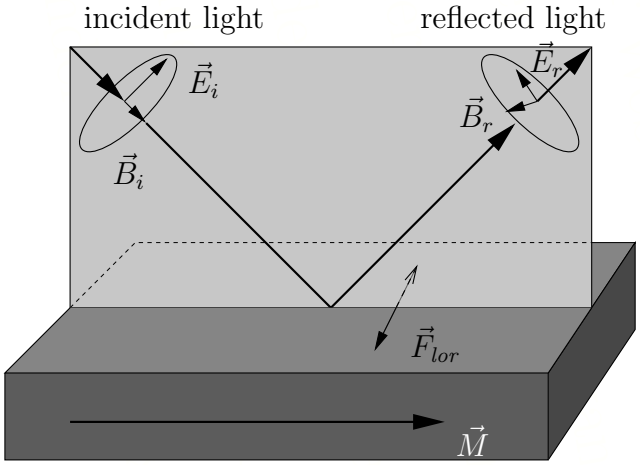

Figure 3.1 – Longitudinal parallel Kerr effect: *Kerr rotation due to the magnetization; The incident light is polarized linearly parallel to the plane of incidence. The reflected light is elliptically polarized as the polarization is rotated backwards.*

light-agitated electrons. In this work we only discuss the case relevant to the situation of the experiments (see Fig. 3.1). The electric field vector is parallel to the plane of incidence (p-polarized), and the magnetization lies in-plane along the plane of incidence. This case is called the longitudinal, parallel Kerr effect. The electric field vector forces the electrons to oscillate parallel to the plane of incidence. As the magnetic field of the sample is parallel to the plane of incidence and parallel to the sample surface, the Lorentz force moves the electrons on an elliptical path perpendicular to the surface and plane of incidence. The field caused by this movement adds to the field of the reflected electro-magnetic wave which results in an elliptically polarized wave.

This is all well for the static case, that is measuring e.g. a hysteresis loop. For the dynamics treated in this thesis (time resolved magneto optical Kerr effect, TR-MOKE), things become more complicated as the initial non-equilibrium in the electron distribution

units	Fe bcc		Co hcp		Ni fcc	
in μ_B	μ_{spin}	μ_{orbit}	μ_{spin}	μ_{orbit}	μ_{spin}	μ_{orbit}
theory	2.1 - 2.2	0.04 - 0.06	1.5 - 1.6	0.07 - 0.09	0.5 - 0.6	0.05 - 0.07
experiment	2.13	0.08	1.52	0.14	0.57	0.05

Table 3.1 – Spin and orbital moments for Fe, Co, and Ni: *Data are taken from [22]. The experimental value for Co was measured on fcc Co.*

acts on $\hat{\boldsymbol{\varepsilon}}$ as well [23]. If we write the Kerr angle $\theta = \theta_{\mathrm{K}} + i\epsilon_{\mathrm{K}}$ as:

$$\theta(t) = FM(t), \tag{3.2}$$

with F being the (time-independent) Fresnel coefficient. If θ would be directly linked to the magnetization only, the Kerr ellipticity should exhibit the same time dependence as the Kerr angle. In this case the following equation would hold:

$$\frac{\Delta M(t)}{M_0} = \frac{\Delta\theta_{\mathrm{K}}(t)}{\theta_{\mathrm{K}0}} = \frac{\Delta\epsilon_{\mathrm{K}}(t)}{\epsilon_{\mathrm{K}0}}, \qquad \text{for all times } t. \tag{3.3}$$

Koopmans et al. presented measurements which showed a clear difference between $\theta_{\mathrm{K}}(t)$ and $\epsilon_{\mathrm{K}}(t)$ during the first 500 fs. Moreover, as Eqn. (3.3) would be valid for all parameters, which are directly dependent on M via the conductivity tensor, several measurements show the failure of this direct link: in [24] the SHG signal undergoes a sign change, while it was carefully verified, that M does not change sign. And a measurement on iron [25] displayed a profound time dependent difference of the MO signal for different probe wavelength up to 100 ps. So we have to rewrite the Kerr angle :

$$\theta(t) = F(t)M(t), \tag{3.4}$$

with an explicitly time dependent Fresnel coefficient. With the assumption, that the excitation of the spins is a weak perturbation to the MO signal, we can write

$$\Delta\theta = F_0\Delta M + M_0\Delta F, \tag{3.5}$$

where the Δ represents the laser induced changes, the index 0 marks the state before the perturbation. The ΔF includes now all optical contributions like e.g. state filling or dichroic bleaching (see Ref. [7, 26]).

With Eq 3.5 it is obvious, that there is no way of separating the optical contribution (ΔF) from the magnetic contribution (ΔM) from an experimental point of view. However, a new theoretical study of the TR-MOKE by Zhang et al. shows, that the temporal difference between the magnetic and the optical response, respectively, does not exceed

50 fs [27].*

3.1.2 Magnetization-Induced Second Harmonic Generation

Another optical approach for measuring ultrafast magnetization dynamics is the magnetization induced second harmonic generation (MSHG) or simple second harmonic generation (SHG). With this technique the frequency doubled part of the reflected probe beam is analyzed. The static SHG is sensitive to the electronic structure, to surface states, and, of course, the magnetization. To account for the transition from linear to nonlinear optics a nonlinear induced polarization is introduced. The linear optical susceptibility $\chi^{(1)}$ is replaced by higher order susceptibilities $\chi^{(n)}$. These nonlinear susceptibilities lead to a frequency conversion [29]. One can write the nonlinear polarization in the frequency domain as

$$\boldsymbol{P}^{(n)}(\omega) = \sum_{\omega=\omega_1+\ldots+\omega_n \text{perm.}} \chi^{(n)}(-\omega, \omega_1, \ldots, \omega_n)\vec{E}_1(\omega_1)\ldots\vec{E}_n(\omega_n). \tag{3.6}$$

The summation is taken over all possible permutations of the sum of the ω_i. In the case of SHG, $(n = 2)$, this yields $\omega_1 = \omega_0$, $\omega_2 = \omega_0$ and $\omega = 2\omega_0$. The electric field of the reflected light can than be written as

$$\vec{E}(2\omega) = \frac{2i\omega}{c}\vec{F}^{(2)}(2\omega)\chi^{(2)}\vec{F}^{(1)}(\omega)|\vec{E}(\omega)|^2 d. \tag{3.7}$$

d denotes the optically active region, that contributes to the SHG. $\vec{F}^{(1)}$ and $\vec{F}^{(2)}$ are the linear and nonlinear Fresnel factors, described in [30].

The magnetization of the sample leads to odd elements in $\chi^{(2)}$ which affect the SHG in two ways. First, a polarization rotation is induced. This is referred to as nonlinear MOKE. This polarization rotation is usually one order of magnitude larger than the linear

*There are different approaches in literature to describe the experimental results concerning TR-MOKE. For example Kampfrath et al. [25] introduce a phenomenological track by expanding the dielectric tensor. Another approach was made with a numerical method based on Green's dyadic technique [28]. With this method the dependence of the Kerr rotation on the wavelength and angle of incidence can be described.

MOKE, but strongly influenced by the electronic temperature [29]. The second influence concerns the total yield of the SHG or MSHG. Here the electronic temperature only adds a background, which can be separated. For this purpose the total SHG yield, $I(2\omega, M)$ is measured for opposite field directions which leads to

$$I^{\pm} = \sqrt{I(2\omega, M)} \pm \sqrt{I(2\omega, -M)}. \tag{3.8}$$

I^{+} scales linearly with the electronic temperature while I^{-} monitors the magnetization [9, 29]. Due to Eqn. (3.8) the even and odd contributions of $\chi^{(2)}$ might be separated, but if the strong disturbance by the pump pulse influences both shares, as it influences the $\vec{F}^{i}$, a pure magnetic signal cannot be received for sure.

3.1.3 X-ray Magnetic Circular Dichroism

X-ray magnetic circular dichroism (XMCD) is a powerful tool to investigate magnetic properties, most of all, because it is element specific. With XMCD the wavelength dependent absorption of X-rays is measured, dependent on the relative orientation of the samples magnetization with respect to the helicity of the X-rays. The great disadvantage is, of course, that one needs a synchrotron as X-ray source. Due to the sum rules linking the polarization dependent p to d transition X-ray absorption intensities to a variety of properties (e.g. the p- and d-shell properties, the charge and the spin density, the orbital momentum orientation, the number of d holes, the magnetic spin moment, the orbital magnetic moment) a lot of information can be gained from XMCD measurements. Explaining all sum rules however fills a thesis on its own. The rules on charge, spin, orbital moment and magnetic geometry can be found in [31]. For ultrafast magnetization dynamics only the sum rules linking spin and orbit are important, which shall be explained in the following.

Let us consider the X-ray induced transitions from the L_3 ($2p_{3/2}$) and L_2 ($2p_{1/2}$) shells to the conduction band (i.e. the d-band). Within the 2p shells the spins are aligned either parallel to the orbit ($2p_{3/2}$, $l \uparrow\uparrow s$) or antiparallel to the orbit ($2p_{1/2}$, $l \uparrow\downarrow s$). Due to selection rules, in a first step the circularity of the incident light acts like a filter for

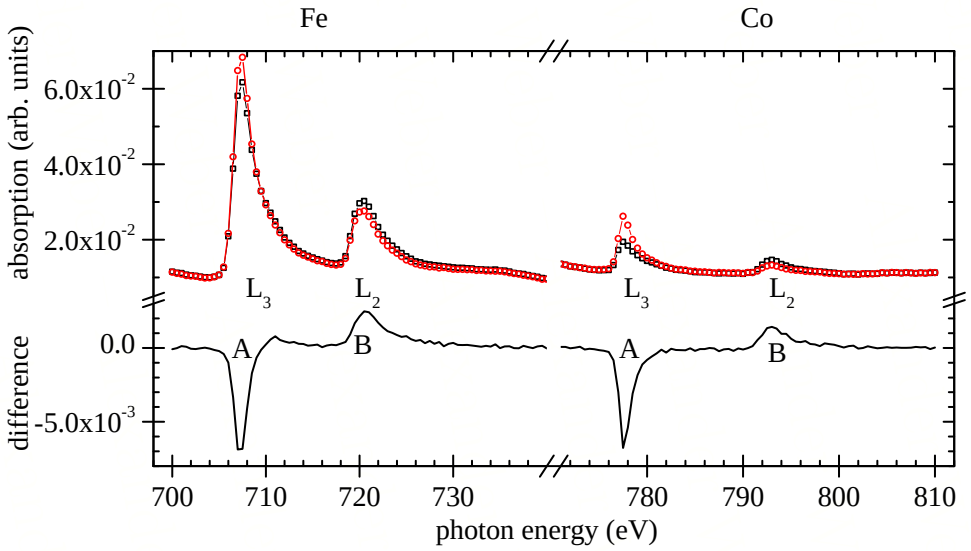

Figure 3.2 – XMCD Spectra for Fe and Co: *Absorption spectra measured on a Cu/CoPd/FeRh/SiN sample at BESSY II at the U-139 UE-56 beamline for femto slicing. The curves represent opposite field (magnetization) directions (squares and circles). The lower lines indicate the difference of the upper curves.*

transitions from the L_2 or L_3 shells. In a second step, if the metal is ferromagnetic, an imbalance in empty spin-up and spin-down states exists in the d-band. Hence, the valence shell acts like a spin detector. Similarly the valence shell will act as an orbital momentum detector if there is an imbalance of states with different magnetic quantum numbers. The summed L_2 and L_3 spectra show a dichroism if the valence shell exhibits an orbital momentum. The difference of the L_2 and L_3 spectra is sensitive to the spin. In short, these are the sum rules for spin and orbit. For the magnetization parallel to the incident beam they can be written as

$$m_l = -2\frac{\mu_B}{C}(A+B), \text{ and} \qquad m_s = -\frac{\mu_B}{C}\sum_{\alpha}(A-2B)|_{\alpha}. \tag{3.9}$$

C is proportional to the square of the p-d-transition matrix element. A and B resemble the areas of the peaks within the difference curve of a XMCD spectra taken with opposite helicity or magnetization(see Fig, 3.2). In the sum rule for the spin a summation over the different directions ($\alpha = x, y,$ and z) is needed.[†]

[†]The above description is taken from [31], where the XMCD effect is explained in great detail.

With these two sum rules one can measure the dynamics of spin and orbit with a stroboscopic setup like used in TR-MOKE. At BESSY II the duration of the X-ray pulses is reduced to 50 fs with a technique called femto slicing. Thus, measurements with good time resolution can be performed [32].

The problem with XMCD was quite analog to the one of TR-MOKE or SHG. The interpretation of the data is based on the sum rules which are derived from the transition matrix. Whether the static transition matrix is still applicable within the ultrafast regime was until recently under discussion. A new theoretical calculation for the transition probabilities [33], however, showed, that the sum rules hold even for the laser excited state, if the full integrals of the peaks are used for the interpretation.

3.2 Photoemission

For the interpretation of the measurements presented in this thesis, it is important to know the area within the band structure from where electrons contribute to the measured photoemission (PE) yield. For this a detailed look into the PE process is necessary.

Photoemission is commonly described by the purely phenomenological three-step model presented in [34]. The PE process is treated in a free electron approximation and divided in three steps: first, the excitation of an electron with energy E_{initial} to a higher state with energy E_{final}. Second, the passage of the electron through the solid to the surface, and finally the penetration through the surface into the vacuum. A detailed description of the theory of photoemission can be found e.g. in [35], or in [36] on a more mathematical basis. The following explanation follows [35].

In the **first step** the electron is excited from the initial state (E_{initial}) to a higher state (E_{final}) within the solid. Energy conservation needs to be fulfilled:

$$E_{\text{photon}} = h\nu = E_{\text{final}} - E_{\text{initial}} = E_{\text{F}} - E_{\text{initial}} + \Phi + E_{\text{kin}}. \tag{3.10}$$

Here E_{F} denotes the Fermi-energy, E_{kin} the kinetic energy of the electron in vacuum, and Φ represents the work function.

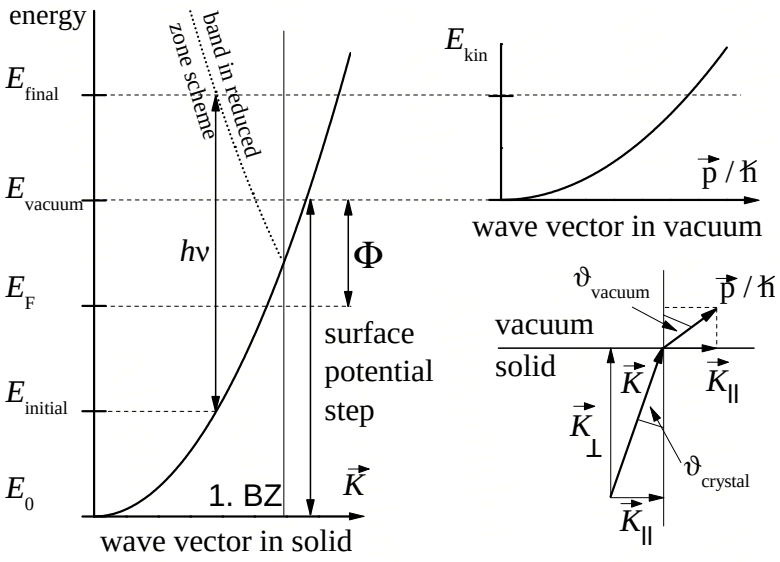

Figure 3.3 – The free electron final state model for PE: *idealized view on the PE process. The vertical line marks the first Brillouin zone (1. BZ). The insert (lower right) reflects Snell's law for an electron passing the surface.*

During the **second step** the percentage of the excited electrons which reach the surface from a depth comparable to the electron mean free path can be estimated as [34, 37]

$$d(E,k) \cong \frac{\alpha\lambda}{1-\alpha\lambda}, \tag{3.11}$$

with the mean free path of the electron, λ, and the optical absorption coefficient, α, its inverse representing the optical penetration depth, $\sigma = \alpha^{-1}$. For visible light σ is in the range of 10 to 20 nm. The mean free path for low energy electrons is considered to be spin dependent in ferromagnets ($\lambda_\uparrow$(Co) = 20 Å, $\lambda_\downarrow$(Co)= 7 Å [38], $\lambda_\uparrow$(Fe)= 16 Å, $\lambda_\downarrow$(Fe)= 4 Å [39]). However, referring to actual measurements on ballistic transport in Fe the difference is negligible [40] for electrons close to the Fermi energy and close to the vacuum energy [41, 42]. To get a rough estimate of the percentage of the electrons, which reach the surface after excitation λ=10 Å is used.

With this approximately 7 % of the excited electrons will reach the surface. The total number of PE electrons saturates at a film thickness of around 10 to 15 nm.

The **third step** needs more consideration, concerning the momentum conservation, which only holds for the component of the wave vector parallel to the surface ($k_\parallel$). For the vertical component the band structure needs to be taken into account. But first we note, that photons with an energy below 100 eV can only excite vertical transitions, as their wave vector, given by $k_{\mathrm{ph}} = 2\pi\lambda^{-1} < 0.05$ Å^{-1}, is negligible compared to the electron

wave vector being up to several Å^{-1}. Within the frame of the three step model the escape cone argument is used to describe the wave vector distribution among the photoexcited electrons. With this the maximum parallel wave vector component can be estimated and thus the region of the band structure relevant for the experiment can be determined. First the perpendicular component of the wave vector (parallel to the surface normal) needs to be large enough to overcome the surface potential step:

$$\frac{\hbar^2}{2m}K_\perp^2 \geq \Phi + E_\mathrm{F} - E_0, \tag{3.12}$$

where E_0 is the energy of the bottom of the valence band. At the surface the parallel components are conserved:

$$\frac{1}{\hbar}\vec{p}_\parallel = \vec{K}_\parallel = \vec{k}_\parallel + \vec{G}_\parallel. \tag{3.13}$$

$\vec{p}$ is the momentum of the electron in vacuum, $\vec{K} = \vec{k} + \vec{G}$ is the wave vector of the photoexcited electron within the crystal in the extended zone scheme. $\vec{k}$ therefore equals the wave vector of the crystal state, $\vec{G}$ the wave vector corresponding to the crystal lattice. Within a free electron approximation, this yields the Snell's law for electrons crossing the surface:

$$\vec{k}_\parallel = \sin\vartheta_\mathrm{vacuum}\sqrt{\frac{2m}{\hbar^2}E_\mathrm{kin}} = \sin\vartheta_\mathrm{crystal}\sqrt{\frac{2m}{\hbar^2}(E_\mathrm{final} - E_0)}. \tag{3.14}$$

The electrons are refracted towards the surface when leaving the crystal. This implies a maximum angle within the crystal ($\vartheta_\mathrm{vacuum} \to 90^\circ$):

$$\vartheta_\mathrm{crystal}^\mathrm{max} = \sin^{-1}\sqrt{\frac{E_\mathrm{kin}}{E_\mathrm{final} - E_0}}. \tag{3.15}$$

This defines the escape cone. With this $k_\parallel^\mathrm{max}$ is defined as well. For the minimum $K_\perp = \frac{1}{\hbar}\sqrt{2m(E_\mathrm{vacuum} - E_0)}$ the electrons escape parallel to the surface. In vacuum the kinetic energy defines the parallel vector component for the limit of parallel escape:

$$E_\mathrm{kin} = E_\mathrm{final} - E_\mathrm{vacuum} = \frac{\hbar^2}{2m}(\vec{K}_\parallel^2 + \underbrace{\frac{p_\perp}{\hbar^2}}_{\to 0}); \tag{3.16}$$

$$\Rightarrow \quad |\vec{K}_\parallel| = \sqrt{\frac{2m}{\hbar^2}E_\mathrm{kin}}. \tag{3.17}$$

With Eq. (3.10) an upper limit for $\vec{K}_\parallel$ can be evaluated.

We will take Fe as an example: For $h\nu = 5.9$ eV and $\Phi(\mathrm{Fe}) = 4.5$ eV [43] the maximum parallel component would be for threshold PE (E_{initial}=E_{F}) $|\vec{K}_{\parallel}| = 0.61$ Å^{-1}. In the reduced zone scheme the maximum wave vectors are 1.55 Å^{-1} in Σ or (110) direction, 2.2 Å^{-1} in Δ or (100) direction, and 1.9 Å^{-1} in Λ or (111) direction. This means, the regions of the band structure perpendicular to the surface normal (the Σ direction in an Fe(110) film) yield only a minor contribution to the PE electrons. As not only threshold electrons can contribute to the process, the perpendicular contribution of the band structure can be estimated to be much smaller than 20 %.

3.3 Spin Analysis with a Mott-Detector

The analysis of a spin polarized electron beam with a Mott detector utilizes the so-called Mott scattering. Sir N. F. Mott presented his calculations on the scattering of relativistic electrons in 1929 [44] based on Dirac's *Quantum Theory of the Electron* [45]. Using the Dirac equation for a free electron the scattering cross section for elastic scattering at a potential is calculated in analogy to non-relativistic scattering theory. The quite lengthy calculation can be found in [46], in [47] the reader will find a condensed overview.

For the special case needed in this work, namely a purely transversal polarized electron beam (e.g. z-direction), the differential scattering cross section into the solid angle, given by θ and ϕ reads [47]:

$$\sigma(\theta, \phi) = |a|^2 \left(1 \pm S(\theta) \sin(\phi)\right). \tag{3.18}$$

Here a includes terms like the spin-flip amplitude, but for the understanding of the detector it can be viewed as a constant. $S(\theta)$ is the so called Sherman function[‡], which depends on the energy of the incident electrons, the scattering material, and the apex angle θ. The + sign applies for a polarization in +z direction (spins down), the − sign for −z (spins up). Eq. (3.18) reveals a "left-right" asymmetry, i.e. for $\phi = 90°$ and 270° the difference in σ is maximum. This means, that in the plane perpendicular to the initial spin polarization the difference in the scattering probability is biggest. In the plane parallel to

[‡]named after Noah Sherman for his calculations of σ in [48]

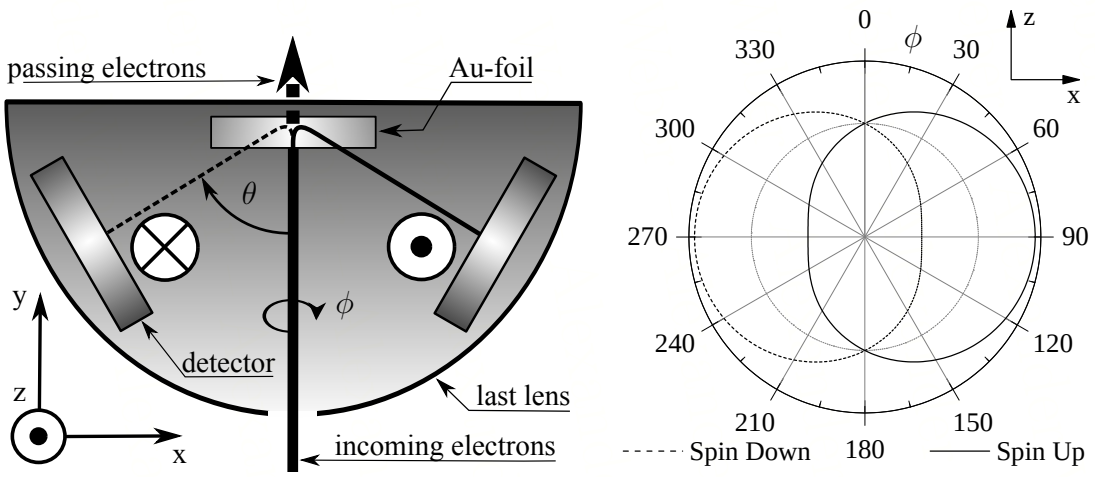

Figure 3.4 – Mott Scattering: *On the left the design of a typical Mott detector is sketched. On the right the scattering probabilities for electrons with different spin orientation is plotted for $S = 0.5$. The y direction points into the page.*

the initial polarization the scattering probabilities are equal (see right frame of Fig. 3.4). As the polarization is defined parallel to the magnetic moment of the electrons and thus antiparallel to the spin, an electron with spin up (along -z) has a higher probability to be scattered to the right.

This can be explained using a simple picture. In its rest frame the electron *sees* the moving charge of the scattering center. So it sees a current and thus a magnetic field witch acts on its magnetic moment. The interaction, analog to spin orbit coupling, is responsible for the angle dependent scattering probability. Besides, the interaction provides a probability to flip the spin of the scattered electron. This however is not important, as for the ϕ-dependence of the scattering-probability only the initial orientation is relevant and the electron detectors them self (the PIPs) do not distinguish the spin directions. For the description of real detectors an effective Sherman function is used. This function consists of the Sherman function described above minus any experimental influences which lead to a reduction of the measured ratio between the two detectors, like e.g. a constant offset in the count rate.

In the section on the measurement procedure (Sec. 6.4, page 52) the derivation of the

samples spin polarization from the measured electron counts is explained.

A new experimental study on the dependence of the efficiency of a Mott detector on the angle of the detectors, the accelerating voltage and their effect on the effective Sherman function can be found in [49].

This concludes the chapter on the experimental techniques. In summary, the results of the optical methods contain a purely optical contribution to the measured signal, which cannot be eliminated for sure. In contrast, the PE with spin analysis provides a direct, unaltered observation of the dynamics of the spin system. The laser induced changes of the conductivity tensor do not influence the outcome. This makes the presented measurement approach an ideal method to determine the true spin dynamics which dominate the magnetism in the 3d-ferromagnets. This, however, is costly achieved by a very long measurement time, counted in days rather than minutes.

4 The Deployment of Ultrafast Magnetization Dynamics

In due course of this chapter an explanation of todays understanding of ultrafast magnetization dynamics will be given. In this respect, however, it does not aim at a complete description of all processes and models in detail, but rather at a nearly chronological summary of the facts that are known and proven with experiments.

4.1 The First Measurements

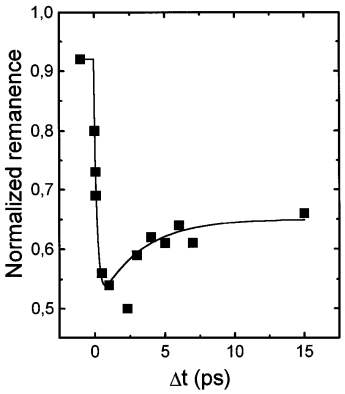

The most frequently shown graph within the field of ultrafast magnetization dynamics can be seen on the left. Beaurepaire et al. published in [11] the first demagnetization measurement performed on a femtosecond time scale: They measured TR-MOKE on 20 nm Ni/MgF_2 (Sec. 3.1.1). This was the initial experiment within the field of ultrafast magnetization dynamics. There followed some measurements on Ni with different techniques, namely MSHG [9] and spin analysis with photoemission (PE) [8]. The latter showed a completely different time dependence than the optical methods. Güdde et al. presented in [50] a first comparison of Ni and Co measured with SHG. This experiment was repeated with a fluence dependence in [51]. The data showed, that after 3 ps the optical response follows the electron temperature [9].*

*Due to the interest in hard-drive recording media a lot of research interest was put to alloys as well, mostly $CoPt_3$ [15, 52–54].

All interpretations of these measurements had in common, that they directly linked the optical response to the magnetization and the electron temperature via the conductivity tensor. Koopmans et al. [55] however showed, that this does not hold. They found a profound difference in the time dependence of the Kerr-angle compared to the Kerr-ellipticity. This difference should not occur, if the magnetic properties are directly linked to the optical response. The differences were found in other measurements as well e.g. in [24] a sign change was found in the SHG-signal and in [25] Kerr measurements with different probe wavelength revealed different signals up to several picoseconds (see 3.1.1).

Around that time Zhang and Hübner [12, 56, 57] came up with the first theoretical description of these fast phenomena, calculating the time dependence of the optical susceptibility tensor. Their theory predicted an intrinsic limit for the optical response of around 10 fs. This was in accordance with the measurements, as the rise time of the first peak therein was believed to be limited by the pulse length (see Tab. 4.1). Their model included no magnetization loss channel, and explained the fast change in the tensor elements with a dephasing of the wave functions. Moreover, Regensburger et al. showed in [24], that a calculation of the electron temperature with the 2TM, assuming a linear dependency of the magnetic tensor element on the temperature, fitted well with their MSHG data. This also showed, that no change in magnetization was needed to explain the strong dip in the MSGH signal. To add to the confusion Zhang and Hübner demonstrated in [58] that in contrast to their earlier calculations the combination of the laser field with the spin-orbit coupling could be responsible for a complete demagnetization within a few femtoseconds. With the title *Ultrafast Magneto-Optics in Nickel: Magnetism or Optics?* of [7] Koopmans et al. put the debate in a nutshell.

Huge effort was put into the separation of the magnetic and the optic signal. e.g. investigating different compounds [60], measuring at different temperatures [26] or measuring with different wavelengths [25]. All attempts revealed a profound difference in the MO response which proofed, that optical methods always measure a non-magnetic contribution. All sorts of purely optic effects could be separated, like acoustic strain waves [23, 61], dichroic bleaching or state filling [7, 26]. But no conclusive way was found to clearly

pulse length (fs)	first peak (fs)	measurement technique	Reference
60	< 1000	TR-MOKE	[11]
150	240	MSHG	[9]
150	200	MSHG	[50]
150	260-280	MSHG	[51]
70	200	TR-MOKE	[55]
150	300	MSHG	[24]
70	200	TR-MOKE	[7]

Table 4.1 – Comparison of different results on Ni: *given is the time delay of the first peak (not the time-constant of the peak, as this depends on the fitting model) dependent on the pulse duration of the laser used. Clearly the duration of the laser-pulse does not alone shape the signal, but, as we know today, the fluence of the pulse [59].*

determine the pure magnetic signal.

A very recent publication [27] might be able to put an end to this debate. In a first principle calculations Zhang et al. calculated the differences between the optical response and the underlying magnetism by splitting up the conductivity tensor. According to their calculation the difference is strongly dependent on the wavelength and duration of the probe pulse. The optical responds is always preceding the magnetism, but only on a scale of 20 fs. On a first glance this contradicts the measurements mentioned above, as profound differences in Kerr angle and ellipticity last up to 500 fs and measurements with different probe wavelength even show differences up to several picoseconds [25]. Further investigation is needed to clearly separate magnetism from optics.

4.2 The Problem of Angular Momentum Conservation

Adding to the question whether the measured signals originate truly in magnetism or if the whole MO response might be a purely optical effect the question of angular momentum conservation arose, as there were no known channels on such short time scales to transport the angular momentum out of the spin system. Spin and orbital moments are related to

the magnetic moment by

$$\vec{\mu} = \mu_{\mathrm{B}}(\vec{L}_{\mathrm{e}} + g\vec{S}_{\mathrm{e}}),\ g \approx 2, \tag{4.1}$$

and the total angular momentum reads

$$\vec{J} = \vec{L}_{\mathrm{e}} + \vec{S}_{\mathrm{e}} + \vec{L}_{\mathrm{p}} + \vec{L}_{h\nu}. \tag{4.2}$$

L_{e} is the orbital momentum, S_{e} is the spin momentum of the electrons. L_{p} is the angular momentum of the lattice or the phonons, $L_{h\nu}$ the angular momentum of the photons of the pump pulse. The total angular momentum is conserved, so a change in $\vec{L}_{\mathrm{e}}$ or $\vec{S}_{\mathrm{e}}$ can only be achieved by a transfer to $\vec{L}_{\mathrm{p}}$ or from $\vec{L}_{h\nu}$ or in between $\vec{L}_{\mathrm{e}}$ and $\vec{S}_{\mathrm{e}}$. Due to the estimation made in [26]†, the angular momentum transferred from the photons is two orders of magnitude to small to be responsible for demagnetization. However, a calculation applied to the experiments of this work, which can be found in the Appendix A.3, shows, that in principle up to 40 % of the demagnetization can be related to the angular momentum transfered from the photons of the pump pulse.‡

To reassess this fact Dalla Longa et al. checked in [63] the dependence of the MOKE signal on the pump beam polarization. On illumination with circular polarized light a sharp peak occurs, dependent on the orientation of the helicity towards the samples magnetization. Dalla Longa et al. constitute this effect as the specular inverse optical Kerr effect according to [64]. However, a change in magnetization direction is equivalent to a change in the helicity of the probe beam. Thus, with this measurement shown in Figure 4.1 an influence on the magnetization by the pump pulse cannot be excluded impeccably.

Moreover, it is possible to directly manipulate the magnetization with circularly polarized light by means of the inverse Faraday effect. This was discovered by Kimel et al. [65]

†this estimation is based on the temperature raise within the electron bath, calculated with the 2TM. However, the failure of the 2TM is, in principle known since 1995 even for non magnetic materials. Groeneveld et al. showed in [62] the failure of the model on Ag and Au and introduced a non-thermal electron model. They stress the important role of e-e-scattering for the e-ph relaxation. This questions any calculation on angular momentum transfer solely based on the 2TM.

‡any geometrical aspect of the incidence of the pump beam towards the magnetization is neglected in this estimation. This will further reduce the amount of angular momentum transfer.

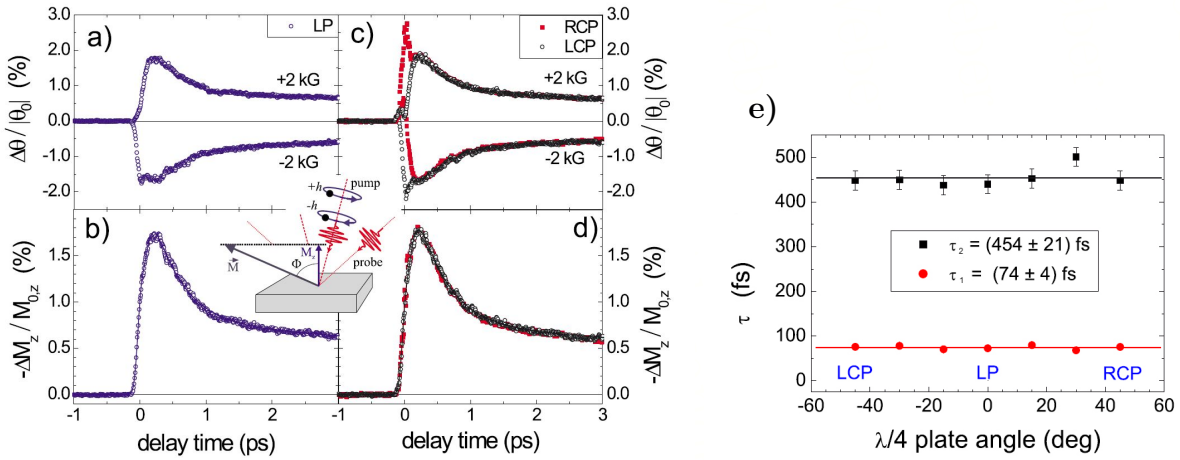

Figure 4.1 – Influence of the Pump Helicity: *K*err rotation measurements for different helicities of the pump beam in opposite fields. a) linear polarized and the difference for opposite fields (b). c) circular polarized and the difference for opposite fields (d). e) related relaxation times. [63]

for media with a strong magneto optic coupling (namely a strong SOC) and is described in e.g. [66, 67]. Beaurepaire et al. [68] observed in 2004 THz radiation induced by the excitation due to the pump pulse. The intensity scaled with the change in magnetization and was always linear polarized, independent of the pump polarization. But they only measured perpendicular to the surface of the sample, which was magnetized in plane. So, due to selection rules, only linear polarized light is expected to be observed.

J.-Y. Bigot et al. [69] studied the pump beam itself regarding its Kerr rotation and ellipticity after reflection from a magnetic sample and found that within the duration of the pump pulse a Kerr rotation and ellipticity can clearly be observed. Moreover they found, that the magnetic field related to the laser pulse can be as large as 1 T in the material.

Summing it up, the demagnetization cannot solely be explained by a angular momentum transfer from the photons, but there are numerous possibilities by which photons might contribute to the effect.

The next possible channel for momentum transfer would be from S_e to L_e. This direct

exchange would be mediated over the spin orbit coupling (SOC). But, due to measurements with XMCD and XAS on Ni, the transfer of angular momentum from the spin to the orbit can be excluded [32, 70, 71], as the spin and the orbit show the same time dependence. However, according to Carva et al. [33], to be sure of this fact, the measurement would need to be repeated with an integral measurement of the peaks, not just the value at one given energy. And in certain alloys, e.g. $Co_{0.5}Pd_{0.5}$, like demonstrated in [72], different time-constants for the spin and orbital momentum of the Co were observed. However, a transfer of angular momentum to the Pd, which has a large orbital momentum compared to Ni or Co, could not be ruled out. Thus, this experiment is not directly comparable to the Ni-measurement. But put together, a small possibility remains for a contribution to the angular momentum transfer within the channel S_e to L_e.

From the above it follows that the angular momentum at large has to be transferred to the lattice. This makes the experiment a kind of ultrafast Einstein de Haas effect. However, the *classical* relaxation times, the transversal and longitudinal relaxation time, are far to slow. This dilemma will be further discussed in Sec 4.3 and Sec 4.4. However, the problem of the angular momentum conservation underlined the question weather the measurements showed any real magnetic behavior at all.

To conclude this section one can say, that the pump pulse might contribute to the angular momentum transfer, and that a possibility remains for a transfer to the orbital momentum. But a new, fast channel for angular momentum transport between spin and lattice is needed to fully describe the dynamics, as we still assume, that a true demagnetization takes place.

4.3 Relation between Short and Long Time Processes

The application of a strong heat pulse was used in a variety of other experiments as well. One goal is to trigger a precessional motion with this disturbance. Due to the heat pulse the magnetization is reduced and the effective local field changes. This cants the magnetization out of its equilibrium position to which it relaxes by a precessional motion.

This precession is described by the Landau-Lifshitz-Gilbert equation (LLG):

$$\frac{\mathrm{d}\vec{M}(t)}{\mathrm{d}t} = -\gamma\mu_0(\vec{M} \times \vec{H}_{\mathrm{eff}}) - \frac{\alpha}{M_{\mathrm{s}}}\left(\vec{M} \times \frac{\mathrm{d}\vec{M}}{\mathrm{d}t}\right). \tag{4.3}$$

The first term describes the precession, the second term the damping of the precession. The damping scales with the phenomenological constant α. Neglecting extrinsic influences, such as defects, α can be explained by spin-orbit coupling, itinerant electrons, eddy currents or direct magnon-phonon scattering [73]. Naturally, a unison or direct combination of this intrinsic damping to the ultrafast demagnetization is tempting.

End of 2005 Koopmans et al. presented a first ansatz which relates demagnetization, the spin precessional decay time, the damping constant α and the Curie temperature T_{C} [74]:

$$\tau_1 = \frac{c_0\hbar}{k_{\mathrm{B}}T_{\mathrm{C}}\alpha}, \tag{4.4}$$

with one additional parameter, $c_0 = 1/4$. The damping parameter α can easily be influenced by doping and it can be determined in a variety of experiments, like ferromagnetic resonance or TR-MOKE [75]. Thus this dependence was well investigated.

For example Pd doped Py (FeNi) show a qualitative agreement with Eqn. 4.4 [76]. On the other hand doping of Ho, Dy, Tb with concentrations up to 8 % can more than double the demagnetization time but changes the damping parameter α even more drastically and in the wrong direction [77]. But as the deduction of Eqn. (4.4) assumes a energy dissipation channel appearing on the short time scale the same way as on longer time scales, rare earth doping seems to be a bad candidate. The magnetization in rare earths stays within the 4f bands, which are almost atomic like, very narrow and barely hybridized. This makes them not comparable to the magnetism in transition metals. Nevertheless, on a long time scale they will contribute to the damping parameter [76].

The connection between ultrafast demagnetization and the precessional motion, however, defines a problem the following way: for nanosecond time scales, where precessional motion takes place, the well established concepts of spin-lattice relaxation work fine [74, 78, 79] and are in accordance even with the concept of the damping in Eqn. 4.3.

On the picosecond and sub-picosecond time scale, however, a new channel for fast angular momentum transfer seems to be open for hot electrons, which obviously does not exist for the precessional motion. This fast transfer of angular momentum can be grasped e.g. by the Elliott Yafet spin flip probability (see Sec. 4.4).

Both mechanisms might be connected in certain systems via Eq. (4.4) by the Curie temperature. This, on the other hand, defines the influence of the exchange coupling between the spins. An explanation could be, that in the case of ultrafast demagnetization, the spins act uncorrelated, independent from each other, and transfer angular momentum more rapidly to the phonon system. Whereas in the case of precessional motion the spins are strongly connected to each other and transfer angular momentum much slower in a collective way.

4.4 Hot Spots and Band Structure

Within due course of this section we try to give an explanation why angular momentum conservation still holds and angular momentum can be transferred more rapidly to the lattice than with the *established* relaxation times mentioned above.

Two assumptions are made to explain the rapid transfer of angular momentum to the lattice. First, in [80] a spin-flip probability α_{EY} for Elliott Yafet (EF) type like spin flips is introduced for each electron-phonon scattering [81, 82]. The Elliot-Yafet mechanism is essentially a Fermi-golden rule mechanism of spin flipping due to impurities or phonons [83]. The interactions are represented by e-e scattering (Coulomb-interaction), and electron-phonon scattering with a scattering rate $K_{\mathrm{e-p}}$ combined with the spin-flip probability α_{EY}. $\alpha_{\mathrm{EY}}= pb^2$, where p is a material constant and b^2 is the degree of spin mixing of the electronic state, see App. A.5 for details. That is, each scattering event is accompanied by a probability for a spin flip, given by α_{EY}, connected with an angular momentum transfer to the lattice. From the possible spin flip mechanisms (Stoner excitations, inelastic spin wave scattering, and Elliott-Yafet spin flips) in [84] and [85] the dominating role of the EF scattering mechanism is emphasized.

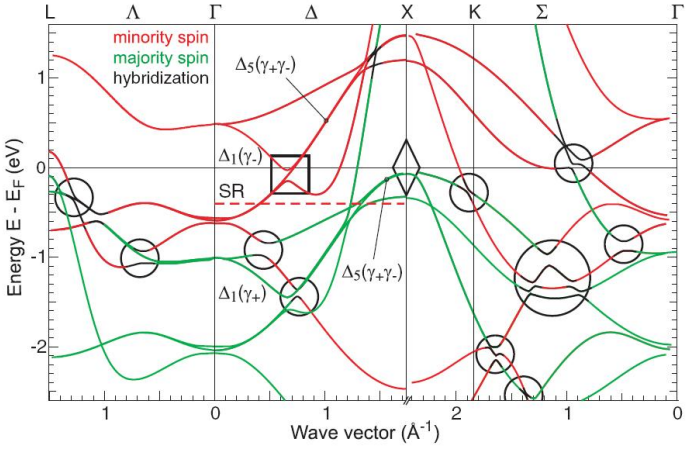

Figure 4.2 – Spin-Orbit Hybridization Points: *Band structure calculation for fcc cobalt. The hybridization points of spin-up and spin-down bands are emphasized with circles (those of bands with equal spin-direction are marked with a square and a diamond). Here the probability for a spin-flip process is highly raised. [86]*

However, $\alpha_{\mathrm{EY}} = 0.01$ was usually estimated one order of magnitude to small to account for a demagnetization on a sub picosecond scale.[§]

For the second assumption the fact, that the magnetic moment for the 3d ferromagnets is dominated by the spin magnetic moment of the conduction electrons [22] plays an important role. This makes it necessary to look at the band structure. However, as a key for the explanation of the dynamics this did not happen until Pickel at al. [86] brought the attention to the band structure with their calculation for Co after the Korringa-Kohn-Rostocker formalism (KKR) [87] in a fully relativistic way, including the spin polarization of the single bands (see Fig. 4.2). With a simultaneous treatment of the SOC and exchange interaction they observed a hybridization of the majority and minority bands. This is where the second assumption comes in: They argue, that at these hybridization points or *hot spots* the spin character of the bands is no longer well defined. This leads to an increase of the spin-mixing parameter b^2 and thus of α_{EY} at these hot spots by at least a factor of 10 [83, 86].

This fact was reassessed by a calculation of the spin mixing parameters for Fe, Co, and Ni from density-functional electron theory [85], which lead to a value of $\alpha_{\mathrm{EY}} = 0.1$. This demonstrates that the EY mechanism in principle is able to describe the fast transfer of

[§]this value was derived for Cu, which is closest to Ni, see [85]

angular momentum from the spin system to the lattice.

Moreover, Koopmans et al. [59] recently presented a theory based on the EY-mechanism which can explain the demagnetization from ultrafast processes like in the ferromagnetic transition metals to slower processes like in rare earth (4f-) materials. Depending on a material specific constant $R \propto \alpha_{\mathrm{EY}} T_{\mathrm{C}}^2/\mu_{\mathrm{at}}$, with μ_{at} being the atomic magnetic moment, the variety of magnetic materials can be sorted into two classes: Type I covers the fast demagnetization like described here, Type II describes processes which show a two-step demagnetization, like in Gd.

Thus, in a band structure with SOC and though hot spots an electron can scatter into a state, which is highly spin-mixed. There the spin-flip probability is highly increased, which leads, depending on the hot-spot density to an overall increase of the spin-flip probability. Thus the rate of angular momentum transfer is mainly given by number of electron scattering events into the hot-spots, which occurs on the same time scale as the electron-electron scattering time [76].

If the assumptions of the Elliott-Yafet spin-flip mechanism and the spin-hybridization points are made a guidepost to the explanation of ultrafast magnetization dynamics is given.

4.5 Summary

To summarize the last sections one can find three central statements:

- The first time constant is fastest for Ni, followed by Fe and Co. The times measured with all optical approaches are in the range of 200 to 300 fs.
- A purely magnetic signal cannot yet be extracted from all optical experiments without any doubts. Even so the magnetization follows the static $M(T)$ curve after 3 to 5 ps, there are differences in the various properties related to the magnetism. Thus it needs to be concluded, that there remain optical contributions up to several picoseconds.

- The concepts of the *classical* spin-lattice relaxation times do not hold on ultrafast time scales. The concept of Elliott Yafet type like spin flip scattering might explain the ultrafast loss in magnetization and the transfer of angular momentum within these short time spans. A transfer of angular momentum from the photons of the pump pulse or a transfer to the orbit might contribute a share to the signal.

5 The Experimental Setup

We performed a classical stroboscopic pump-probe experiment on samples prepared and measured in situ. The pump pulse (840 nm) was used to strongly excite the electronic system, the probe pulse (210 nm) for the photoemission of the electrons. Their spins were analyzed with a Mott detector. In order to perform the experiments a chamber for molecular beam epitaxy (MBE) was designed and built and the measurement chamber was redesigned to fit the special requirements of the experiment. An overview of the setup is shown in Fig. 5.1. First, the UHV-system, containing preparation and measurement facilities, will be presented. Subsequently the laser-system will be described. As an introduction to the experiment the pump-probe technique is explained in the appendix.

5.1 The UHV-system

The whole setup can be divided into the UHV-assembly containing sample preparation and measurement, and the laser-system.

Starting with the UHV-chambers we had one preparation chamber with a load lock connected, an evaporation chamber and the measurement chamber. The preparation chamber supplied facilities for Ar-ion-sputtering, sample heating with an e-beam heater and an oxygen inlet for the O_2-treatment of the tungsten crystal. Additionally, an Auger-electron-spectrometer (AES) for sample characterization and an electron gun for low energy electron diffraction (LEED) for the surface analysis were attached. The preparation chamber was pumped with an ion-getter-pump (IGP) and a turbo-pump which ensured

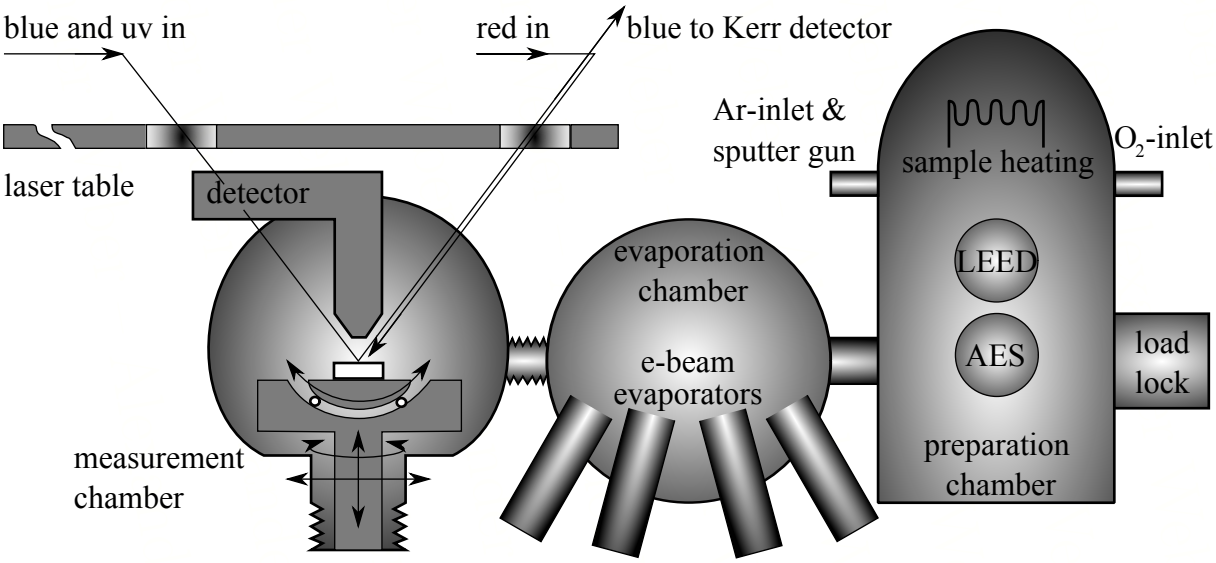

Figure 5.1 – Setup Overview: *schematic illustration of the main setup. The measurement chamber was mounted sturdily to the laser table and was connected to the neighboring chamber with a flexible bellow. The reflected blue beam exited the chamber trough the entry window of the red beam and was used for MOKE measurements.*

a base pressure of 1×10^{-10} mbar.

With a transfer rod we could move the samples to the evaporation chamber. Here four e-beam evaporators were mounted. One silver evaporator for capping layers, one for iron, one for nickel, and a fourfold evaporator filled with iron, cobalt, and nickel as backup. The sample was placed close to a water-cooled quartz micro balance (QMB), running at 6 MHz, to monitor the growth rate. The QMB was calibrated with the AES with a reproducible thickness accuracy of 0.2 monolayers (ML). The evaporation chamber was solely pumped with an IGP. The base pressure achieved was around 2×10^{-10} mbar and reached 4×10^{-10} mbar during evaporation. Details of the sample preparation are given in the appendix, A.1.

5.2 The Measurement Chamber

The measurement chamber was accessible with the same transfer rod used to transfer samples from the preparation chamber to the MBE chamber. The chamber was pumped

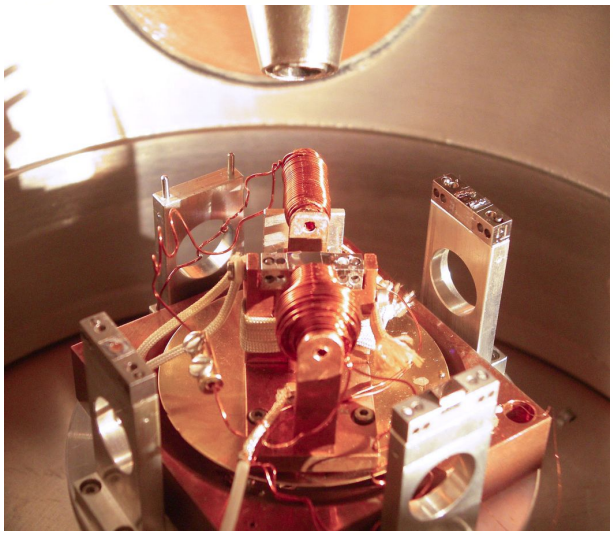

Figure 5.2 – The Setup around the Sample: *Picture of the surroundings of the sample: The first collection lens can bee seen at the top. The sample is placed on a heatable, fully pivoting stage, between two small air coils.*

with an IGP, additionally the lens system of the Mott-detector was pumped with a second small IGP. This allowed us to separate the part including the detector with a valve, if the main chamber needed to be opened for maintenance.

The base pressure in the chamber was between 6×10^{-11} mbar and 1×10^{-10} mbar. A good pressure was mandatory for the experiment, as already 1.5 ML of Oxygen are enough to reduce the spin polarization by a factor of three to four [88].

Fig. 5.2 shows a picture of the setup within the measurement chamber. The sample was placed between two small air coils which yielded fields up to 120 Oe. The whole stage allowed translational and rotational movement in all degrees of freedom. The x-y-translation was controlled with stepper motors for easy scanning of the sample. The z-translation and rotation around the z-axis was done manually with a linear and a rotational feed through. The rotational degrees of freedom around the x- and y-axis were realized by three fourfold scanning piezo crystals placed underneath the sample mount.

At an angle of 30° with respect to the sample surface normal two windows equipped with achromatic lens systems allowed the incidence of the pump and the probe beams from opposite directions (see Fig 5.3).

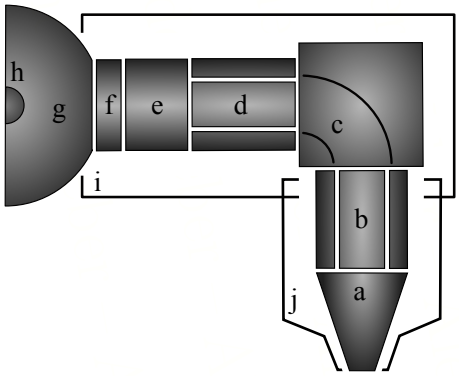

The electrostatic lens system (left picture) for the collection and focusing of the photoemitted electrons was mounted with 90° to the plane of incidence and with 45° to the surface normal. The distance of the first lens to the sample was about 4 cm. After the first collection lens (a) a quadrupole (b) allowed to focus the beam into a 90° -deflector (c). Another quadrupole mounted after the deflector (d) and a focusing unit (e, f, g) completed the lens system in front of the Mott-detector (h). The parts (c) to (f) were covered with mu-metal from the outside (i). To shield the parts (a) and (b) a mu-metal shield was mounted inside the chamber (j).

The detector itself (h), described in [89] and Sec.3.3 was at a positive potential of 45 kV to give the electrons enough kinetic energy in order to achieve a reasonable Sherman function. It consisted of a gold foil surrounded by four electron detectors, so called PIPS, that is "particle implanted silicon diode". The PIPS were connected to pre-amplifiers, a discrimination unit, and opto-couplers. The opto-couplers were connected to a counter-card mounted in a PC via optical fibers. They were necessary, because the whole electronics of the detector unit was floating at 45 kV as well. With the Mott-detector mounted in the given geometry we were able to monitor one in plane spin polarization (perpendicular to the plane of incidence) and the out of plane component.

5.3 The Laser System

The requirements of the pump probe experiments include a laser system with certain specifications. The pulse length should be short enough to reveal the underlying dynamics. The pulse power needs to be fairly high to ensure a strong disturbance of the electron system by the pump pulse and some reserve for the generation of the probe pulse by frequency doubling. Moreover, the repetition rate should be moderate to prevent a dc heating which would decrease the dynamic signal. We used a combination of a Ti:Sapphire

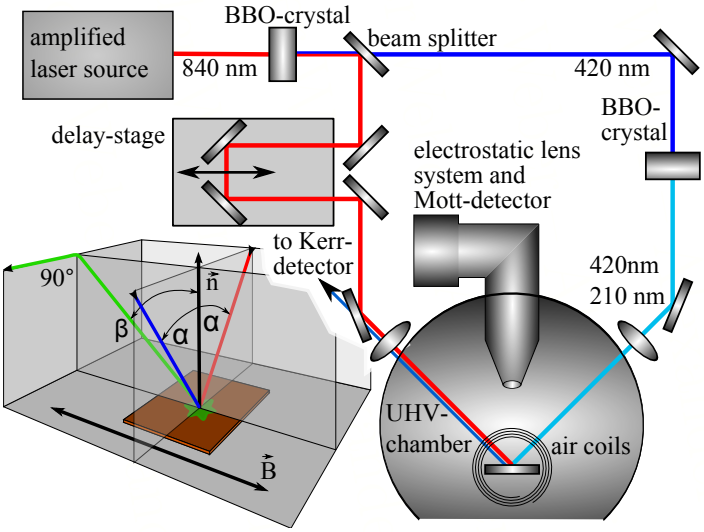

Figure 5.3 – Pump Probe Setup and Measurement Geometry: *Illustration of the experimental setup. the geometry is shown in the lower left. The angles of incidence for the pump and probe beams are $\alpha = 30°$, the angle of the lens system is $\beta = 45°$ with respect to the sample surface normal.*

laser* and a Ti:Sapphire based regenerative amplifier,† both running in near infra red, at 840 nm. This supplied us with pulses up to 4.3 µJ pulse energy at a repetition rate between 25 and 250 kHz. The pulse length was about 220 to 250 fs full width at half maximum (FWHM) and thus the limiting factor for the time resolution of the experiments. We used the system at a repetition rate between 25 and 76 kHz which provided us pulses with a fluence up to 13 mJ cm^{-2}, while preventing dc heating on the metal substrates.

The pump-probe scheme is depicted in Fig. 5.3. The amplified beam was focused onto a β-barium-borate crystal (BBO) for frequency doubling. The two shares (840 nm will be referred to as *red* and 420 nm as *blue* for simplicity) were separated by a dichroic beam splitter. The red beam, used as pump, traveled over a motorized translation stage to be able to adjust the pump-probe delay. The blue beam was frequency doubled again with another BBO crystal, resulting in a weak share of 210 nm UV-light of up to 2 µW cw-power, used for photoemission. Both beams were focused onto the sample with achromatic lens assemblies. We ensured, that the pump focus size was around twice the size of the probe focus, which guaranteed a homogeneously excited probing region. Before the second frequency doubling a combination of a $\lambda/2$ plate with a polarizer allowed a rotation of the polarization direction without any loss in power. The pump beam path was equipped

*Mira 900, Coherent

†REGA 9000, Coherent

	wavelength nm	energy ($h\frac{c}{\lambda}$) eV	focus ⌀ µm	pulse length fs	max. fluence $mJ\,cm^{-2}$	energy / pulse µJ
red	840	1.48	60	250	13	0.7
blue	420	2.95	30	250	2	0.03
uv	210	5.9	30	350	2×10^{-3}	0.2×10^{-3}

Table 5.1 – Beam Parameters

with a $\lambda/2$ plate or a $\lambda/4$ plate, respectively, to check any dependency of the incident polarization of the pump beam.

The last mirror in the red path, directing the pump beam into the measurement chamber, was designed in a way, that it reflected the pump beam to ≈100 %, but the 420 nm part of the probe beam was split into two equal shares. One of which was, due to the geometry, directed opposite the pump beam and used to adjust the spatial overlap of the pump and probe beam with the aid of two pinholes within a square-millimeter. This allowed us to monitor both beams with a Questar far field microscope on the sample surface. The other part of the probe beam was used to measure the Kerr-rotation. The fine adjustment of the overlap will be described in Sec. 6.2.

6 Adjustment and Measurement

This chapter will describe the adjustments and optimizations necessary for obtaining any results and the methods used to determine the focus sizes as well as the pulse duration and the focal overlap. An explanation of the measurement procedure will conclude the chapter.

6.1 The Mott-Detector

The most crucial and most delicate part of the experiment was the Mott-detector and the electrostatic lens system. Here two specific settings need to be explained because of the paramount influence they have on the outcome of the experiments.

First, the discrimination levels of the electron detectors have to be considered as they directly affect the effective Sherman function. They define the threshold charge* of the detector currents, on which it depends whether a peak is counted or not. To ensure, that each electron is counted, one has to accept a certain number of *dark counts*. That is the count rate, without any electrons reaching the detectors. This will give a small offset to the counts and therefore reduce the effective Sherman function.

The second important calibration is the average count rate, that is the number of electrons reaching the detectors per second. It is easily adjusted by tuning the UV-power. The detectors can only respond to one electron per pulse. If two electrons reach one detector within a very short time interval, such as the pulse duration, only one electron

*The discrimination unit integrates the current over the time, which gives the charge

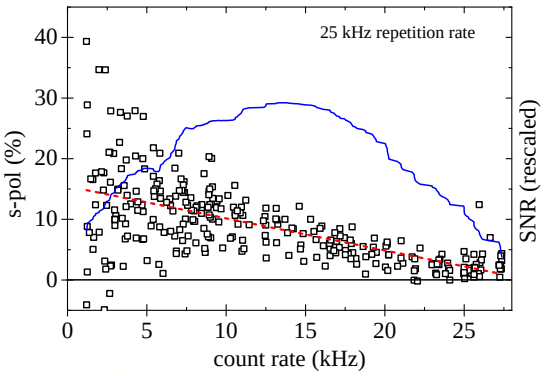

Figure 6.1 – Spin Polarization vs. Count Rate: *For each count rate the number of electrons was counted for the same time. The red dashed curve is a linear fit. The blue line gives the signal to noise ratio for the spin polarization.*

will be registered. This implies, that the number of electrons per time needs to be smaller than the repetition rate of the laser. Otherwise the detectors are saturated. This, too, has a direct influence on the measured spin polarization. Fig. 6.1 shows the dependence of the measured spin polarization on the count rate. The graph was taken with the laser operating at 25 kHz repetition rate. When the count rate reaches the repetition rate the detectors for opposite spin directions are both close to saturation, and will therefore yield the same number of electrons. Thus the spin polarization drops to zero. With a very low count rate, the spin polarization is large, but so is the variance, if the time interval for the count recording is kept constant. For a count rate a little above half the repetition rate the best SNR is attained.

6.2 Spatial Overlap and Focus Determination

For the determination of the spatial overlap of the pump and the probe beam first of all the electron optics were optimized for each new sample. Once the counts were optimized the spin-polarization was tested. The point of incidence of the blue beam was marked on a telescreen, which pictured the sample surface through a Questar far field microscope. However, in spite of only using achromatic lenses after the second BBO, the focus of the UV-beam was separated from the focus of the blue beam by ≈70 µm. Thus the position of the UV-focus needed to be determined separately. For this purpose the sample was replaced by a thin Cu-disk containing a pinhole with 100 µm in diameter. The height of the Cu-disc was adjusted with the aid of the point marked for the position of the

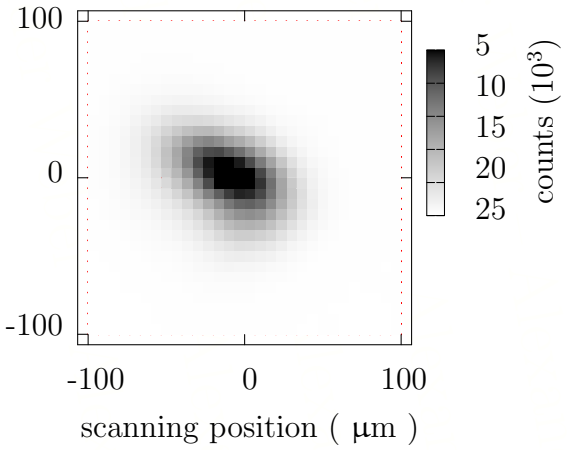

Figure 6.2 – Scanned Image for the Determination of the UV Focus Position: *A copper disc with a pinhole was moved point by point underneath the UV beam. The image consists of 30 × 30 points. For each point the total yield of photoemitted electrons was measured.*

blue focus on the telescreen. A lateral scan of the sample while recording the number of photoemitted electrons yielded a minimum at the position of the pinhole (Fig 6.2). The sample stage was then moved to this minimum which ensured, that the pinhole was exactly at the position of the UV-focus. As the pinhole was visible through the microscope, its position and thus the position of the UV-focus could be marked on the telescreen as well. Returning the sample and readjusting the height, now the red beam was adjusted on the label referring to the UV-beam. This guaranteed the spatial overlap of the pump and the probe beams within an uncertainty of half the focus diameter.

The focus diameter for the UV beam could be calculated by deconvoluting the pinhole from the scanned image. For the determination of the focus diameters of the red and the blue beams the procedure above was repeated, but in stead of the Cu-pinhole a Au-

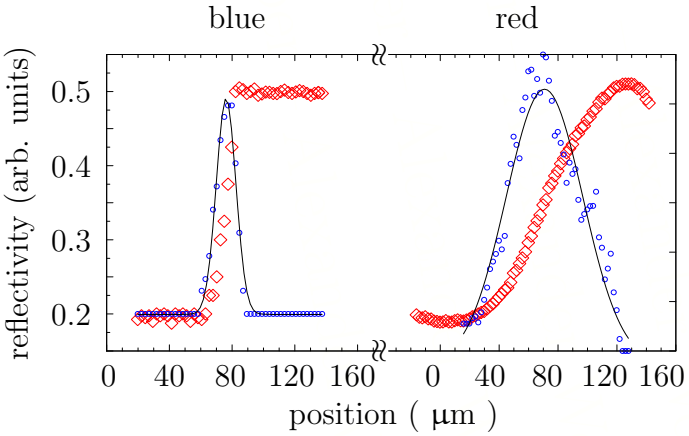

Figure 6.3 – Determination of the Focus Diameters: *A structured sample was scanned while the intensity of the reflected beam was measured. The squares show the signal measured, the circles show the smoothed derivative and the line the Gaussian fit.*

structure on GaAs was used and the reflectivity was recorded, instead of the count rate (Fig 6.3). The determined values for the diameters can be found in Table 5.1 on page 44.

6.3 Determination of the Pulse Length

The determination of the pulse length of the initial red beam was a straight forward matter, as the adjustment procedure of the laser amplifier included the adjustment of the pulse length with an optical compressor. The pulse length was hereby monitored with an autocorrelation device.[†] As the pulse length was around 250 fs the influence of any optics in the beam path could be neglected (thin lenses a.s.f.).

The pulse length of the blue beam was determined with two methods. First, the blue and red beam were focused to a clean tungsten crystal. With the work function of tungsten being larger than the energy of the blue photons, 2PPE could be applied to measure the time dependent cross-correlation between the blue and the red pulses by changing the delay between the two pulses. This can be applied, because the lifetime of the intermediated state during the 2PPE is of the order of 10 fs [91]. The resulting electron yield can be seen in Fig 6.4. The flatter trailing edge on the right is due to an already high fluence of the red pulse, which leaves some excited electrons for a time span around the thermalization time (10 % of the pulsewidth). Fitting different pulse shapes yields a range for the pulse duration of (250±5) fs, see Tab. 6.1. This was carried out for different pulse lengths of the red beam and the blue pulse duration always matched the red one. (The above mentioned value was the shortest measured.)

The second method applied was the measurement of the TR-MOKE and reflectivity signal on Fe. As the MO response and the reflectivity are known to be faster than the pulse length, the result in our case can be approximated as a convolution of a step function (the optical response) with the pulse shape. The results can be viewed in Chap. 7. Both

[†]In an autocorrelator the beam is split in two equal parts which are both focused on a frequency doubling crystal with a variable delay between both. The intensity of the frequency doubled light depends on the delay. This is used to determine the pulse length.

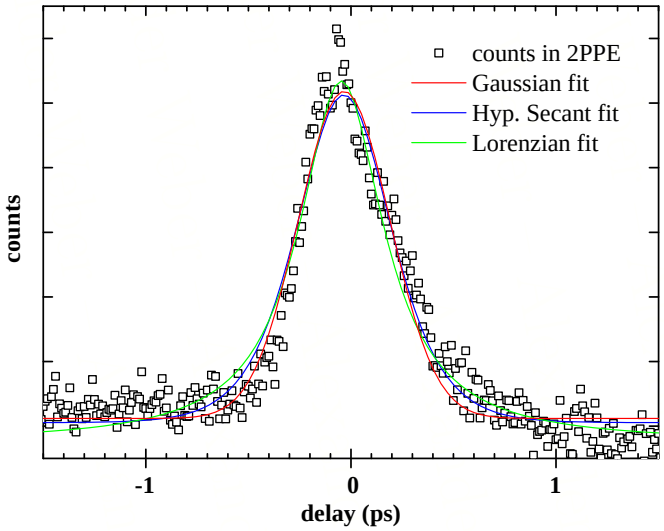

Figure 6.4 – Electron yield in Crosscorrelation red-blue: *2PPE electron yield depending on the temporal overlap of the red and the blue pulse. Standard model pulses are fitted to the curve.*

techniques yield the same results of ≈250 fs (See Tab. 5.1). Of course both methods can just estimate the pulse length, but the precise match of the results militates in favor of the correctness of the value.

The first method was applied to determine the UV-pulse length as well. A small dip in the number of counts during the overlap of the pump and the (UV) probe beam was interpreted in analogy to the cross-correlation of the red and the blue beam. However, the dip is very small, less than 5 % in most cases. Thus the results are noisy and vary, depending on the fit-function and the measurement between 0.3 and 0.5 ps. An example is plotted in Fig 6.5. Moreover, the dip does not always show in the same direction and was observed in opposite direction as well by Heitkamp et al. in CoPt-multilayers [92]. The origin of the dip is yet unknown which makes this method questionable. Nevertheless, it was the only working way of estimating the duration of the UV-pulse.[‡]

[‡]we tried 2PPE on an oxidized W-crystal as well (work function > 6 eV) but without success.

Function		$\frac{\tau_p}{\tau_{ac}}$	τ_p (fs)
name	formula		
Gaussian	$e^{-\frac{4\ln 2t^2}{\tau_p/2}}$	0.707	252
Hyperbolic secant	$\mathrm{sech}^2(\frac{1.76t}{\tau_p})$	0.648	246
Lorenzian	$\frac{1}{1+\frac{4t^2}{\tau_p^2}}$	0.5	251

Table 6.1 – Typical Pulse Shapes: *The table shows common model pulse shapes [90], the correction factors for autocorrelation and the resulting pulsewidth of the blue beam from the cross-correlation red-blue. Due to the manufacturer the hyperbolic secant should fit the pulse shape of the used amplifier, the REGA 9000, best.*

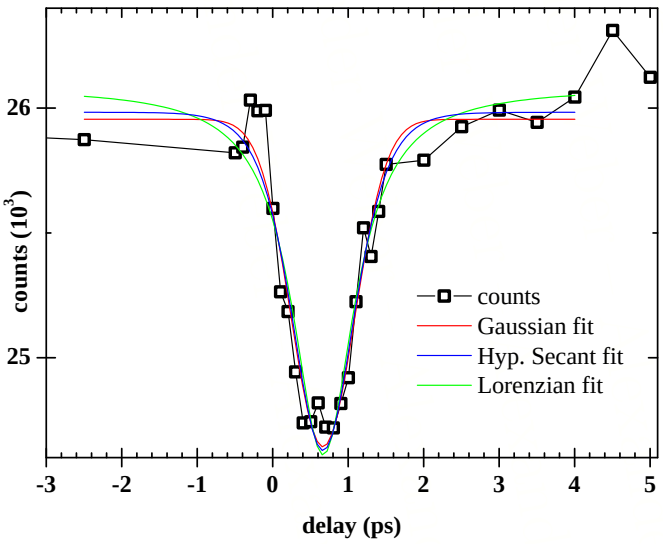

Figure 6.5 – Change in electron yield during pump-probe overlap: *The pump pulse reduces the count rate by 5 %. This small dip was used to determine the UV-pulse length in analogy to the pulse duration of the blue beam. The different fits were evaluated for multiple measurements and average between 0.3 and 0.5 ps.*

6.4 Measurement Procedure

Before we go to the results chapter it is necessary to explain the exact measurement procedure, which was applied for the dynamic spin-polarization measurement. Before the main measurement could be started the above described adjustments were carried out. A stable operation of the laser was mandatory. The overlap of the pump and the probe beams and optimized settings of the lens system were important requirements to assure that the spin polarization was within the expected range. This took several days for each measurement, including the film growth and the focus determination.

During the measurement itself the following procedure was applied:

1. move the translation stage to the proper position for the desired pump probe delay;
2. close relay which connects the coils to the current supply;
3. saturate the sample with a short field pulse;
4. open the relay and short circuit the coils to ensure that no field is applied, which would influence the path and spin orientation of the PE electrons;
5. count the electrons reaching the detectors for a given time t;
6. close relay and saturate the sample in opposite direction; open relay;
7. count the electrons for the opposite field for the time t;
8. repeat steps 2 to 7 n times;
9. move the translation stage to the next position (step 1);

The coils were connected over a relay which disconnected the current supply and short-circuited the coils, to make sure, that during the counting period the field at the sample was zero. We used field pulses of 120 ms duration. This allowed us to apply fields up to 120 Oe with very small air coils. According to [93] the duration is still long enough to avoid any change in size and shape of the hysteresis loops during the switching.

The counts of each detector were artificially separated into two channels, in order to get an estimate of the error within the statistic. This separation was triggered by an

external frequency generator. This will not be included in the following derivation of the spin polarization, as it would just double the number of variables. And to simplify things more, we just consider two channels, i.e. one polarization axis.

During step 5 the electron detectors for e.g "up"(↑) and "down" (↓) will send each counting event to the counter card, which will add the events up to the values $C_\uparrow$ and $C_\downarrow$. This is done for opposite field directions, + and −. So we end up with:

$$C_{\uparrow,+} \text{ and } C_{\downarrow,+} \tag{6.1}$$

during step 5, after applying the field in +direction, and

$$C_{\uparrow,-} \text{ and } C_{\downarrow,-} \tag{6.2}$$

during step 7, after applying the field in the opposite direction, the −direction. The asymmetry between $C_{\uparrow,i}$ and $C_{\downarrow,i}$ is defined as

$$A_i = \frac{C_{\uparrow,i} - C_{\downarrow,i}}{C_{\uparrow,i} + C_{\downarrow,i}}. \tag{6.3}$$

A_i can contain a system asymmetry, $A_i = \hat{A}_i + A_{\text{sys}}$, that is the A_i's need not to be symmetric around zero. Thus $A_+ + A_-$ needs not to be zero but equals $2A_{\text{sys}}$. This was the reason, besides the better SNR, for measuring with opposite fields. By taking the difference, $A_+ - A_- = \hat{A}_+ + A_{\text{sys}} - \hat{A}_- - A_{\text{sys}}$ the system asymmetry drops out. Remembering Eq. (3.18) from Sec. 3.3, a 100% polarized electron beam would yield

$$C_{\uparrow,i} \propto |a|^2(1 + S) \tag{6.4}$$

counts on the one detector and

$$C_{\downarrow,i} \propto |a|^2(1 - S) \tag{6.5}$$

counts on the other detector (ignoring a system asymmetry). Using Eqs. (6.4) and (6.5) in Eq. (6.3) it is clear, that for a 100% polarized beam the measured asymmetry A_i equals the Shermann function S. The true spin polarization P of the beam can be calculated

from the measured values, $C_{i,j}$, as

$$\begin{aligned} P &= \frac{A_+ - A_-}{2S} \\ &= \left(\frac{C_{\uparrow,+} - C_{\downarrow,+}}{C_{\uparrow,+} + C_{\downarrow,+}} - \frac{C_{\uparrow,-} - C_{\downarrow,-}}{C_{\uparrow,-} + C_{\downarrow,-}} \right) \frac{1}{2S}. \end{aligned} \tag{6.6}$$

The difference $A_+ - A_-$, considering the possible system asymmetry, requires the division by two. The division of the Sherman function yields the spin polarization, as can easily seen by inserting Eqs. (6.4) and (6.5) into Eq. (6.6).

For the Mott detector used in the experiments the Sherman function was determined to be 0.15. This was done with an 100 % polarized electron beam on an identical system [89, 94].

7 Results and Conclusions

In the following chapter the results of the spin-polarization measurements and conclusions thereof are presented. First the results of the Fe films are displayed, followed by the Co-samples. The attempts to measure Ni and to use other substrates than tungsten are discussed briefly before a summary concludes the chapter.

Before we start the report on the results the reader shall be reminded on the meaning of the fit functions used here: The response of the sample is treated as

$$R(t) = 1 - \left[A \left(1 - e^{-\frac{t}{\tau_1}} \right) e^{-\frac{t}{\tau_2}} + B \left(1 - e^{-\frac{t}{\tau_2}} \right) \right] H(t) \tag{7.1}$$

for short time intervals. This function is a solution of the 2TM [15]. It will be referred to as 2 exponentials fit (2EF). For longer time intervals the second term in Eq. (7.1) is expanded by a third exponential function, $e^{-\frac{t}{\tau_3}}$ like described in Sec. 2.3 on page 11. This will be referred to as 3 exponentials fit, or 3EF.

7.1 Iron Films on Tungsten - Fe/W(110)

Our first successful dynamic spin polarization measurement is shown in Fig. 7.1. The initial in plane spin polarization (first short plateau) is around 27 % which fits well with the expected spin polarization for Fe, being 26 to 31 % for electrons down to 1.5 eV below Fermi energy [95]. This value is determined, like described in the last chapter (Chap. 6.4) by subtracting the asymmetry values for opposite fields and dividing them by two times the Sherman-function (Eqn. 6.6). After the excitation by the pump pulse the

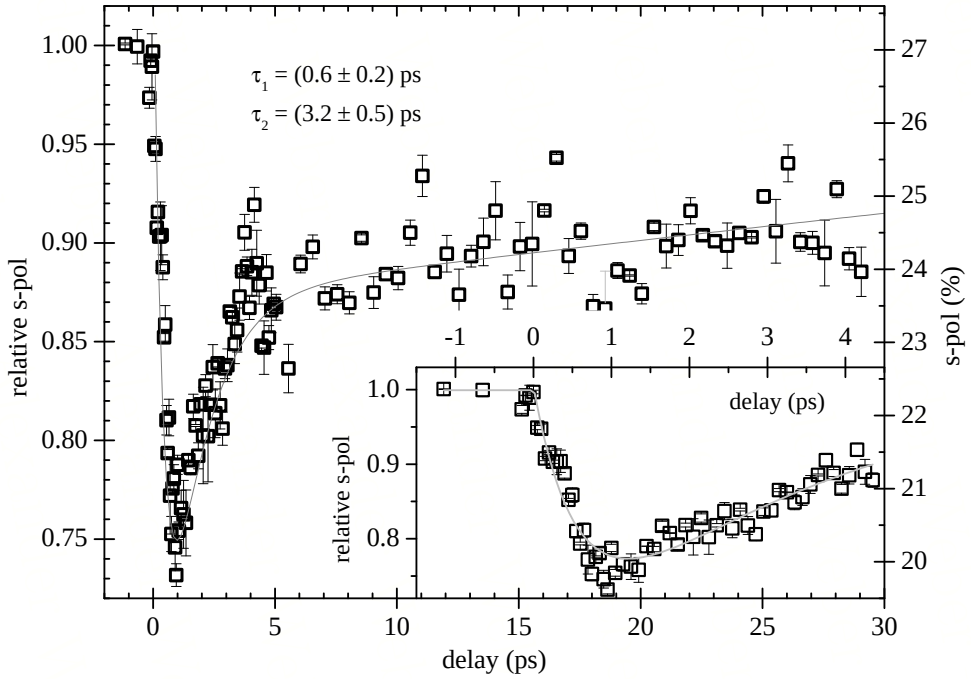

Figure 7.1 – Example Measurement: Fe/W(110): *Our first successful dynamic measurement with a Mott detector. The pump power was 27 mW corresponding to 7 mJ cm^{-2}. The measurement took about 12 hours, for each point approximately 6 million electrons were counted. The error bars represent the standard deviation. The right axes shows the measured s-pol, the left axis the normalized s-pol. The insert shows the first 4 ps.*

spin polarization (s-pol) is reduced by more than 25 % to a value of 20 % polarization. This minimum is reached ≈0.9 ps after the s-pol starts to drop, which will be referred to as zero in time and is determined by the according fit. This corresponds to $\tau_1 = (0.6 \pm 0.2)$ ps. After the minimum the s-pol recovers fast to 85 % of its initial value within 2 ps, $\tau_2 = 3 \pm 0.5$ ps. The relaxation past the 3 ps shows a time constant of $\tau_3 = 200 \pm 50$ ps, which is the order of magnitude of the spin-lattice relaxation time [11, 78, 79, 96]. The overall behavior is quite like it is expected from TR-MOKE measurements. And, quite unlike the s-pol measurements reported in [8], in our experiments the s-pol always recovers completely to its initial value. This recovery is strongly fluence dependent (as shown in Fig. 7.4).

It shall be stressed here, that all measurements were done in remanence with the mag-

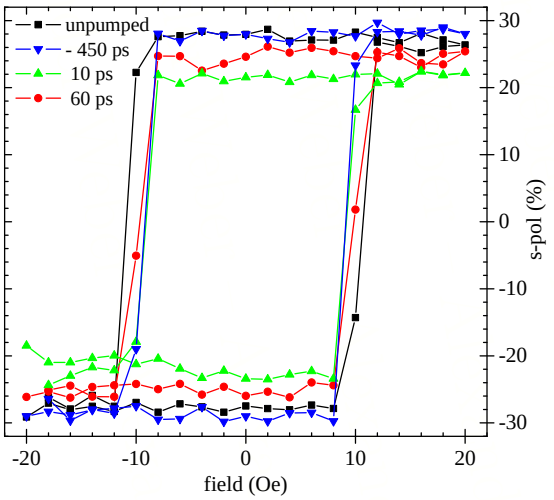

Figure 7.2 – Fe/W(110) Hysteresis Loops measured in remanece: remanent s-pol values are shown, measured without the pump pulse and for different delay times at a pump power of 8.7 $\mathrm{mJ\,cm^{-2}}$.

netic field switched off during the measurement. The s-pol is derived from the remanent asymmetries for opposite fields. The polarization of the pump beam was perpendicular to the plane of incidence, the polarization of the probe beam was tilted 45° to the plane of incidence.

For each measurement great care was taken, that no dc heating was caused by the pump pulses. This was further ascertained by taking a hysteresis loop* without the pump pulses present and comparing it to a loop taken with the pump pulses set to a negative delay (see squares and triangles in Fig. 7.2). With hysteresis loops also the amount of quenching of the s-pol was reassessed.

Fig. 7.3 shows a strong dependence of the amount of quenching on the fluence of the pump pulse, which was measured for a large spread of pump powers. The range varies from a reduction of the s-pol up to 40 % for a fluence of 8.7 $\mathrm{mJ\,cm^{-2}}$ down to only 5 % for 1.1 $\mathrm{mJ\,cm^{-2}}$.

In Fig. 7.4 the measurement was repeated for selected fluences on a longer time scale and with higher statistics. All measurements have in common, that a first very fast drop ($\tau_1 \approx 0.6$ ps) in the s-pol is followed by a relatively fast recovery ($\tau_2 \approx 1.5$ ps). A second, much slower recovery brings the s-pol back to its initial value ($\tau_3 \approx 100$ ps). The insert

*strictly speaking, as the hysteresis loops are also measured after switching off the magnetic field for each point, they are no real hysteresis loops, but recorded remanence values after a field pulse of the given strength.

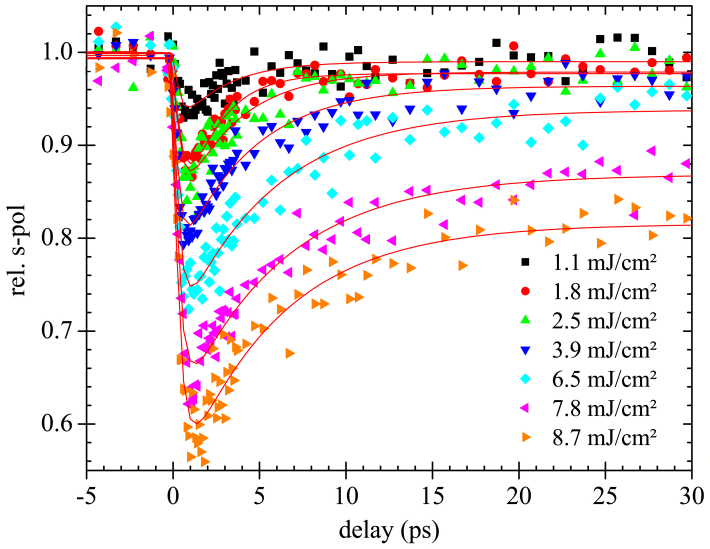

Figure 7.3 – Fluence Dependent S-Pol Dynamics for Fe: *The graph shows the s-pol dynamics for various fluences. The curves are normalized to their initial, maximal value. The red lines show the fit according to the Two Temperature Model (2TF).*

of Fig 7.4 shows, that the time delay of the minimum is around 1 ps and only weakly dependent on the fluence as far as it can be seen within the measurement uncertainties. From the measurements with a low fluence it can be nicely seen, that the s-pol recovers back to its initial value. (For measurements with higher fluence the complete recovery was always verified for delay times of 4 ns.) This behavior is known from TR-MOKE data and fits well with the 3EF. The dependence of the reduction of the s-pol on the pump fluence is linear. This can be seen in Fig. 7.5. The linear dependence for the quenching of the s-pol fits accurately with the values derived from TR-MOKE measurements made on Fe/MgO by Carpene et al. [97] (blue squares).

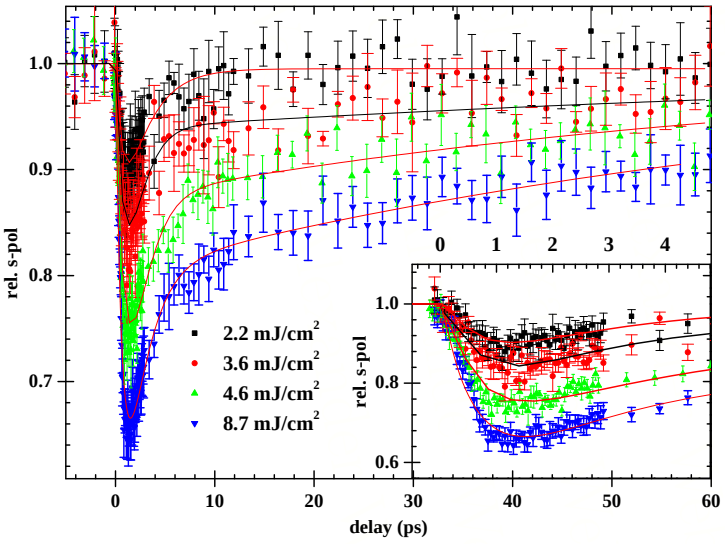

Figure 7.4 – Fluence Dependent S-Pol Dynamics for Fe on a long time scale: *The graph shows the s-pol dynamics for various fluences. The curves are normalized to their initial, maximal value. The insert shows the first 12 ps together with the fit curves according to the 3EF.*

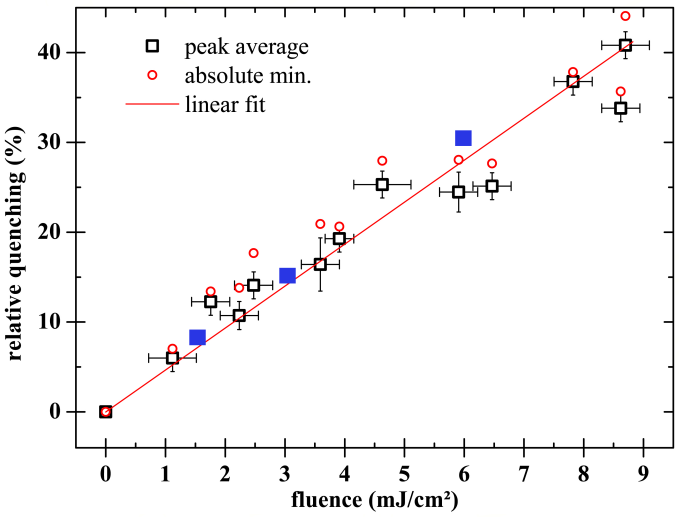

Figure 7.5 – Fluence dependency of the s-pol quenching: *The relative amount of the reduction in the s-pol is plotted vs. the fluence of the pump beam. The squares represent the average value over the points within the peak, the circles the smallest value measured. The blue squares are the values for Fe/MgO from Carpene et al. [97].*

The dependence of τ_1 on the amount the s-pol is quenched, like suggested by Koopmans et al. [59], is shown on the left hand side of Fig 7.6. The circles and squares indicate the values derived from two sets of measurements. The large error-bars of the one series (circles) show, that the values for τ_1 derived from the fits are highly uncertain, as a lot

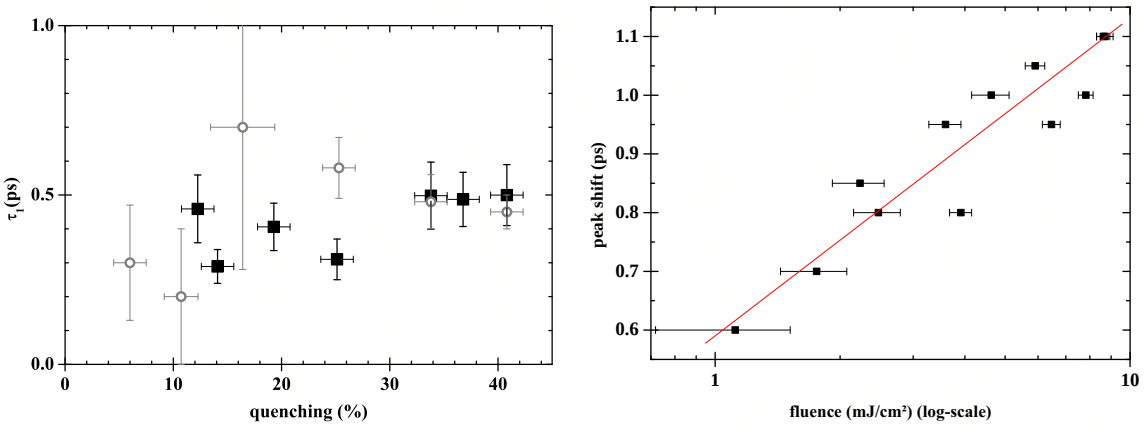

Figure 7.6 – Fluence Dependence of τ_1: *On the left hand side the values for τ_1 derived from the 2EF are plotted versus the amount the s-pol is quenched, for two sets of measurements (squares and circles). The squares show a flat dependence with a slightly higher values for higher fluence or quenching, respectively. On the right hand side the delay until the s-pol is quenched maximal is plotted versus $\ln \rho_f$ which shows a linear dependence.*

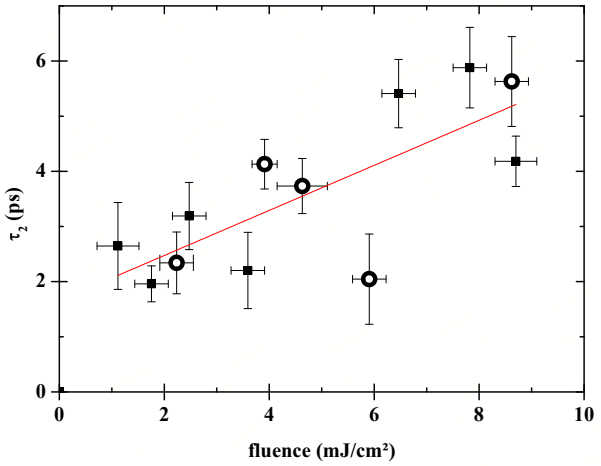

Figure 7.7 – Fluence Dependence of τ_2: *The relaxation process, τ_2, exhibits a slight linear dependence on the fluence of the pump beam. The circles mark the measurements from Fig. 7.4.*

of parameters, like the zero time, strongly influence the values of τ_1. Therefore, on the right hand side of Fig. 7.6 the time delay until the s-pol is reduced maximal is plotted versus the logarithm of the pump fluence ρ_f. From this it is clear, that this delay-time is proportional to $\ln \rho_f$. However, with the available time resolution limited by the pulse length to around 250 fs, a slight increase of τ_1 to higher fluences can be observed, which is in agreement with the prediction of Koopmans theory [59]. But it is still noticeable, that even the average over all measurements of τ_1=(0.45±0.15) ps is much larger than the values measured with TR-MOKE on Fe/MgO [97]. Carpene et al. found values from 0.05 to 0.075 ps increasing with the pump fluence for values between 1.5 and 6 mJ cm^{-2}.

In contrast to τ_1, the second time constant, τ_2, describing the first relaxation or recovering process, is easier to fit and not so highly sensitive to the other fit parameters. Thus, as shown in Fig. 7.7, a weak linear dependence on the pump fluence can be found. This, again, is in good accordance with [97]. But here as well, the s-pol is much slower than the TR-MOKE-response of the literature: $\tau_{2-\mathrm{spol}} \approx$ 2-4 ps and $\tau_{2-\mathrm{TRMOKE}} \approx$ 0.9 ps. From the data plotted in Fig 7.4 the third time constant, τ_3, could be determined for the highest three fluences. It varies from 80 ps for 3.6 mJ cm^{-2} to 120 ps for 8.7 mJ cm^{-2}. With these values it can be addressed as the spin-lattice relaxation time, as it fits exactly in the range mentioned in literature [11, 78, 79, 96].

The s-pol measurement was compared with a TR-MOKE measurement carried out on the same sample. For the TR-MOKE the sample holder was rotated by 90° to achieve

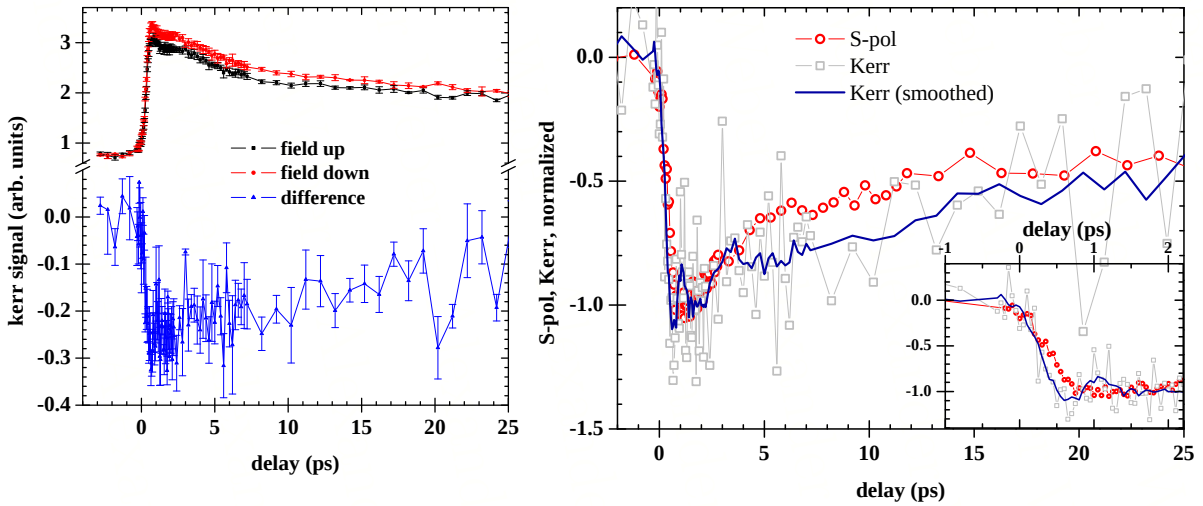

Figure 7.8 – Comparison of Kerr with S-Pol for Fe: *On the left two TR-MOKE measurements are shown, taken with opposite fields. The difference of both measurements (blue) is used on the right hand side for comparison with the s-pol data. Here the circles show the normalized s-pol, the squares show the normalized Kerr-signal. The blue line is a smoothed plot of the Kerr-difference.*

a longitudinal geometry and the wavelength of the probe beam used was 420 nm. The results are shown in Fig. 7.8. The Kerr measurement shown in the graph is the difference of the two Kerr signals recorded with opposite fields, $\theta_K(\uparrow)-\theta_K(\downarrow)$ (left hand side). Both measurements were made with a fluence of 8.7 $\mathrm{mJ\,cm^{-2}}$ of the pump beam. Two profound differences can be found. First, within the error the 2EF fit of the Kerr data reveals a much shorter decrease of the Kerr signal than the s-pol data. The times τ_1 differ by more than a factor of 2: $\tau_{1,\mathrm{s-pol}} = 0.65 \pm 0.15$ ps and $\tau_{1,\mathrm{Kerr}} = 0.25 \pm 0.2$ ps. The insert clarifies the difference during the first picosecond. Second, between 3 and 15 ps after the pump pulse the s-pol shows a faster relaxation than the Kerr-signal which is most probably due to the large error within the TR-MOKE measurement.

As the rise time of the Kerr signal is expected to be much shorter than our pulse length, according to the measurements of Carpene et al. [97], this measurement was used as well, to have a comparison to the determination of the probe pulse duration with the two photon photoemission, described in Sec. 6.3. As the TR-MOKE measurement shows a

rise time of 0.25 ps both measurements are in good agreement. In comparison with [97] the TR-MOKE measurement shows clearly the limitation of the time resolution due to the pulse duration. The Kerr-signal is limited by the experimental resolution. On the other hand, the s-pol signal is more than two times slower. Thus, this comparison shows, that the s-pol results are not limited by the time resolution of the experiment. Moreover, the estimated time resolution based on the calculations in the Appendix A.4 show, that the presented values of τ_1 are not just the result of a broadening due to the probe pulse. And, the results for Co (Sec. 7.2) are far from the limitations and show an even larger τ_1.

To summarize the results on Fe there are three major facts:

- Time resolved spin polarization measurements do yield results comparable to the results with all optical strategies. The overall curve shape as well as the fluence dependence of the amount of quenching and of τ_2 match the results of MO data.
- The values for τ_1 and τ_2 are large in the s-pol measurements compared to the MO measurements.
- τ_3 could be determined as (100±20) ps. This value fits in the estimated range of the spin-lattice relaxation time.

7.2 Cobalt films on tungsten - Co/W(110)

The dynamic behavior of the s-pol in Co is qualitatively the same as the one in Fe. In Fig. 7.9 an exemplary measurement is shown. Again, it was carefully checked with hysteresis loops that there occurred no dc heating (right hand side). Noticeable is the considerably slower response of the s-pol compared to the iron one: $\tau_1 = (1 \pm 0.5)$ ps in Co and 0.6 ps for Fe.

This value is, again, larger than the values obtained with optical approaches. Güdde et al. report a value smaller than 500 fs at 12 $\mathrm{mJ\,cm^{-2}}$ for measurements with SHG [50], Cinchetti et al. observe the minimum at a delay of 700 fs for 10 $\mathrm{mJ\,cm^{-2}}$ with TR-MOKE [84], and Heidkamp et al. observe the minimum at a delay of 400 fs at 8 $\mathrm{mJ\,cm^{-2}}$

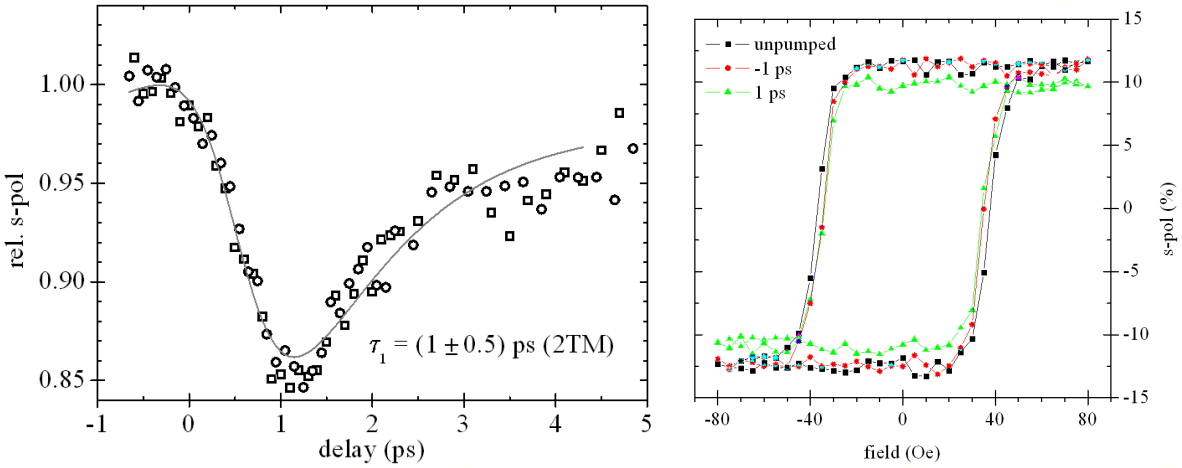

Figure 7.9 – Spin Dynamics on Co/W(110): *The graph on the left shows two independent measurements (circles and squares) carried out with 9.5 mJ cm^{-2}. On the right hysteresis loops are shown analog to the one of iron.*

with 2PPE [92].

The dependence of the amount of quenching on the fluence is again linear, as shown in Fig. 7.10. The values match the values of other measurements made on Co thin films within the measurement uncertainties. The red squares show values of the quenching from measurements with a fluence in a critical region. For fluences within this region the s-pol does not recover to its initial value, even after blocking the pump pulse (see Fig 7.12 and the text later on page 65).

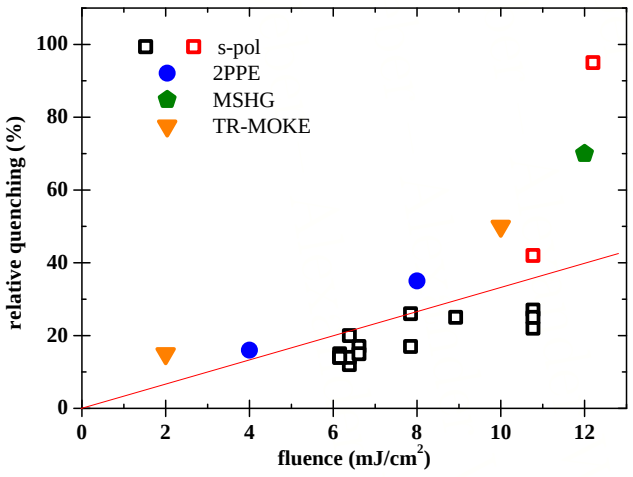

Figure 7.10 – Fluence dependence of the quenching for Co: *The graph shows the fluence dependent amount of quenching for different measurement approaches. black squares: s-pol, red squares: s-pol with no full recovery, blue circles: 2PPE [92], green diamond: MSHG [50], orange triangles: TR-MOKE [84]*

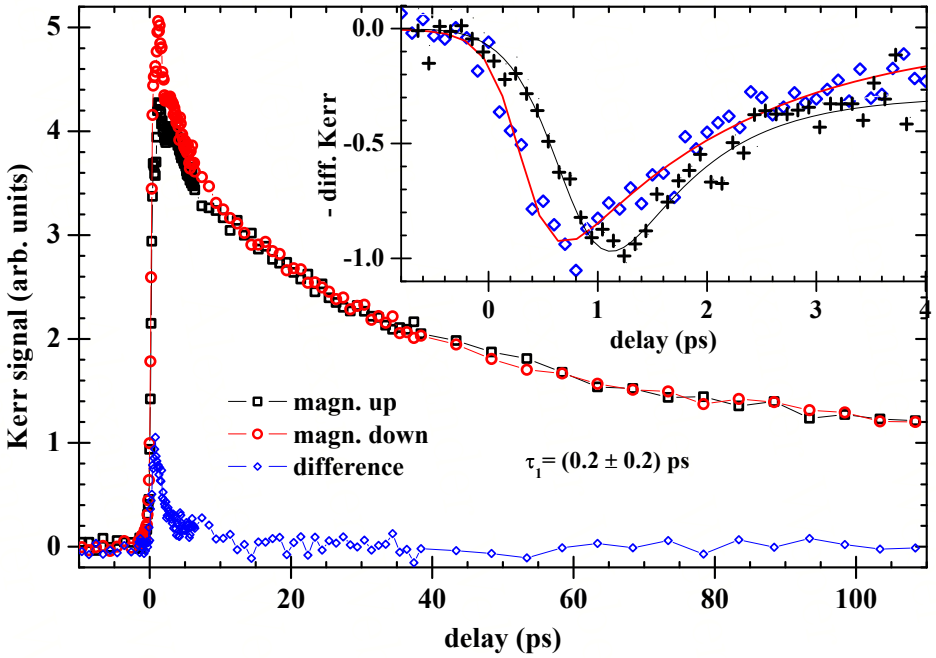

Figure 7.11 – TRMOKE on Co/W(110): *Time resolved Kerr measurement for opposite field directions. The diamonds indicate the difference of the two Kerr measurements. The insert shows the first 4 ps of the difference with opposite sign. A spin polarization measurement is plotted in crosses for comparison.*

In Fig 7.11 a TR-MOKE measurement is plotted. The dynamics reveal a large signal in the MOKE but this signal is only slightly dependent on the sign of the applied field (huge optical background). The difference of the MOKE signals for opposite field is plotted in the insert for the first 4 ps together with a s-pol measurement. Both measurements were made with the same parameters. The comparison reveals a huge difference in the times until the curves are minimal. In the case of Co the s-pol response is even 5 times slower than the optical response ((1 ± 0.5) ps vs. (0.2 ± 0.2) ps). Again, for the TR-MOKE measurement the sample was rotated by 90° compared to the s-pol measurements to attain a longitudinal geometry.

The measurements on cobalt turned out to be much more difficult than the one on iron. For one, the observed spin polarization for Co was smaller than the one for Fe. This made the SNR much smaller. Second, the prepared Co films were much more inhomogeneous.

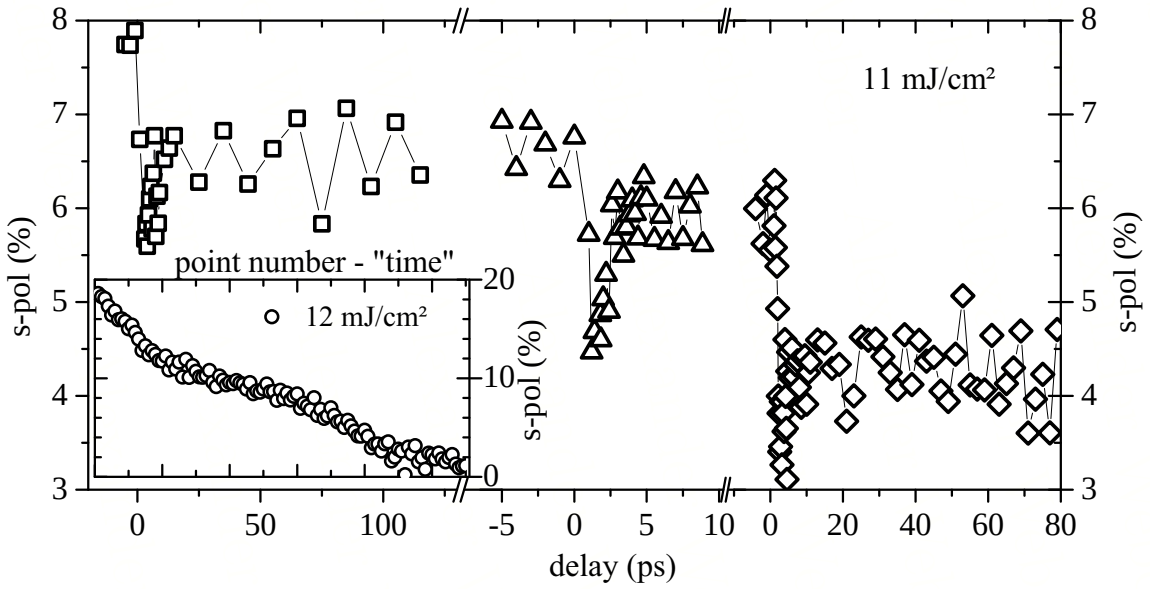

Figure 7.12 – Permanent Destruction of Spin Polarization: *The data were taken directly after each other with the same parameters. The spin polarization is reduced stepwise, the overlap of the pump and the probe pulse triggering the decrease. The insert shows a continuous decrease of spin polarization down to zero, independent of the pump probe delay, if the fluence is increased even more.*

There were large areas which showed no spin polarization at all. Moreover, there were areas with a highly reduced work function, which lead to a high number of photoemitted electrons due to the pump pulse. Moreover, for Co a strong dependence of the PE efficiency on the polarization of the red beam was observed. The measurements where carried out with an incident polarization of the pump beam chosen to yield minimal *red* counts. This was achieved for the polarization being tilted by 45° towards the plane of incidence. Another problem was to find the right fluence for Co. Due to the low signal to noise ratio a relatively high fluence was needed to yield proper data. But this lead to another problem: the used fluences were close to a regime, were the spin polarization is quenched permanently, which is discussed in the following.

Fig. 7.12 shows what happens, if the fluence is increased into a critical region. The overlap of the pump and the probe beam, involving a slightly higher energy deposit than the pump beam alone, triggers a stepwise, permanent reduction of the spin polarization. If

the fluence is increased even more, the spin polarization decreases with the exposure time to the probe beam, independent of the pump probe delay, which is shown in the insert of Fig. 7.12. This behavior can no more be interpreted as dynamics, but a permanent destruction of the local spin polarization, as it does not recover after blocking the pump beam. The curve looks surprisingly like the curve presented by Scholl et al. in [8]. This underlines the importance to verify a complete recovery of the s-pol for each measurement e.g. with hysteresis loops.

The behavior cannot easily be explained. And, as it is not a dynamic effect, it will be omitted in the further discussion. A structural change within the Co-layer or at the Co-W interface may be the reason for the vanishing of the magnetization. Further investigation is needed in order to find the true origin of this permanent *switch-off* of the s-pol.

Summary of the results on Co:

- $\tau_1 \approx$ 1 ps and thus much larger than in Fe.
- The fluence dependent amount of quenching fits with the results found in literature for MO strategies.
- In Co the s-pol can be reduced stepwise or quenched permanently if the pump fluence is sufficiently high.

7.3 Other Systems: Nickel, MgO, and GaAs

It shall be mentioned briefly, that we tried to measure Ni/W(110) and Fe/MgO(100) as well. However, both measurements where unsuccessful. The small air coils, mounted in the measurement chamber, could not supply the field necessary to switch the magnetization in Ni. At room temperature at least 190 Oe are required for switching a Ni thin film [98]. This rendered the attempts to measure Ni with our setup useless, as the field achieved with the air coils was limited to 120 Oe.

The idea to use MgO as substrate arose for two reasons. First, to refine the understanding of the Three Temperature Model (see 2.2) it would help to separate heat diffusion due

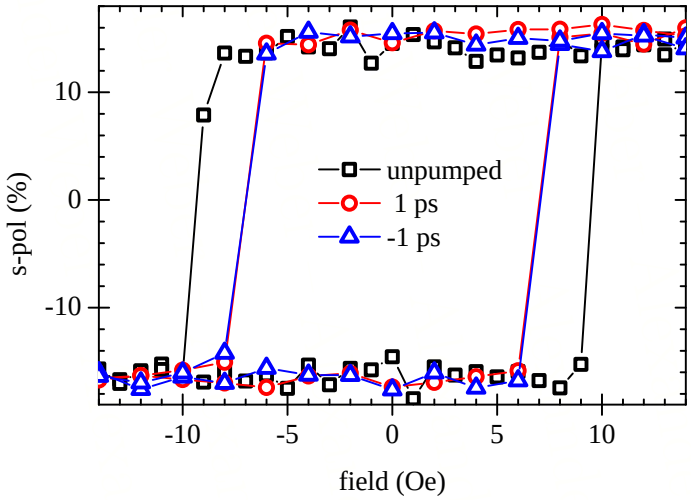

Figure 7.13 – Hysteresis loops for Fe/GaAs: *the graph shows three hysteresis loops measured in remanence. The curve measured with negative delay does not match the unpumped curve, but the curve with 1 ps delay.*

to hot electron transport from heat diffusion due to phonons. A dependence of the MO response on the substrate was already observed and the influence of the transport of hot carriers out of the probed region even on the sub-ps time scale was already stressed out [99]. Thus, using an insulator as substrate would have allowed to exclude all effects of hot electron transport into the substrate. And the relatively high heat conductivity of MgO (for an insulator) would have provided enough heat transport due to phonons in order to prevent any dc heating.

Second, Fe grows on MgO with a (111) surface. Thus, the measurements on MgO would have allowed the probing of a different region of the Fe k-space.

For the experiments the MgO single crystals were fixed on a sample holder with tantalum foil. A thin layer of conducting silver was applied to one edge of the crystal to prevent a charging of the sample. During the degasing at elevated temperatures up to 800°C , part of the MgO surface got covered with the conducting silver, but leaving an area large enough for the measurement. Nevertheless the electrical contacts to the surface were unreliable and the count rate of the PE electrons were very unstable. No reliable measurement was possible. A structured contact, e.g. with Au and a bonding to the sample holder might circumvent the problem, but was not applied within the work.

For the latter reasons the system Fe/GaAs(001) is of interest, too, as here Fe grows with a (100) surface. This, again, would allow to probe a different region of the band

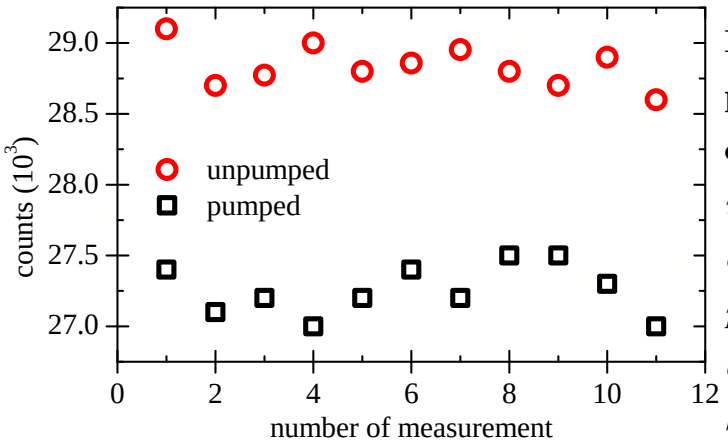

Figure 7.14 – Influence of the pump pulse on the average count rate for GaAs: *The number of PE electrons per time is clearly reduced by the presence of the pump pulse. This effect might be due to an increased influence of the Schottky barrier.*

structure. Additionally, the growth of around 10 ML shows a good uniaxial anisotropy, with coercive fields below 10 Oe. The GaAs wafers used were highly doped, so there were no problems with the conductivity. However, the attempt to measure s-pol dynamics with GaAs as substrate was unsuccessful. We believe the reasons for this were twofold: First, the heat conductivity of GaAs is poor. Fig. 7.13 shows hysteresis loops measured in remanence. Unlike the measurements on the W-substrates the curve measured with a negative delay does not match the unpumped curve, but the curve measured with 1 ps delay. Thus, the deposited heat of the pump pulse lead to dc heating. Noticeable is the absence of a reduction in the s-pol. In return the remanence is reduced by the influence of the pump pulse. Second, the band gap of GaAs exactly matches the wavelength of the pump pulse. This could lead to a depletion of electrons at the Fe surface due to the Schottky-Barrier between the Fe and the GaAs. This would result in a reduction of photoemitted electrons. Indeed a 7 % reduction of PE electrons could unmistakably be addressed to the pump beam, as is shown in Fig 7.14.

To summarize this, with the pump beam on, the s-pol did not change in value, but the coercive field decreased slightly. This was verified with Kerr measurements. Moreover the pump beam reduced the number of photoelectrons. Both effects were independent of the pump probe delay, apart from a small dip in the counts during the overlap, as described in Sec. 6.3. So no dynamics could be observed.

7.4 Summary and Conclusion

The first thing to be mentioned is, of course, that it has been shown that time resolved spin polarization measurements are possible and do yield results comparable to the results with all optical methods.

The s-pol is a direct measure of the magnetism in 3d-ferromagnets. Thus, its reduction implies a true reduction of the spin-magnetic moment within the heated area. As the amount of reduction dependent on the fluence of the pump pulse is equal for the MO and s-pol measurements, respectively, this shows, that the MO response does indeed contain a true magnetic contribution. Thus, the question *magnetism or optics?* can be partly answered: Yes, there is a change in magnetism.

However, the question remains, how much optical effects contribute to the MO signal and on which time scales. And, why are the s-pol measurements slower?

For the second question the time of travel of the electrons could be considered. The electrons travel from the excited region through the film during which they could mix with "younger" electrons excited closer to the surface. Electrons with an energy of 5.5 eV travel at a speed of 1.6 $\times 10^6$ m/s. However, if one considers even a 20 nm thick film, the time of travel is as short as 12 fs.

Another reason could be found in any effects of dichroic origin, like the MCD or MLD, which would influence the polarization of the photoexcited electrons. But it can be viewed in [100], that any such effect could only be observed in special geometries, which differ from the one we used in the experiments.

If there are remaining optical effects a further possibility could be a fast, strong optical peak. As a fast response due to ΔF underlying the MO response cannot be ruled out in all measurements for sure this could yield a fast contribution to the MO data. This, we believe, is indeed the case, if the MO response shows a second broad peak after the first sharp one. However, by carefully designing the experiments one can get rid of such a behavior, e.g. by taking the difference signal for opposite fields. Then the curves look identical to the s-pol ones but are faster. This, together with the calculations in [27],

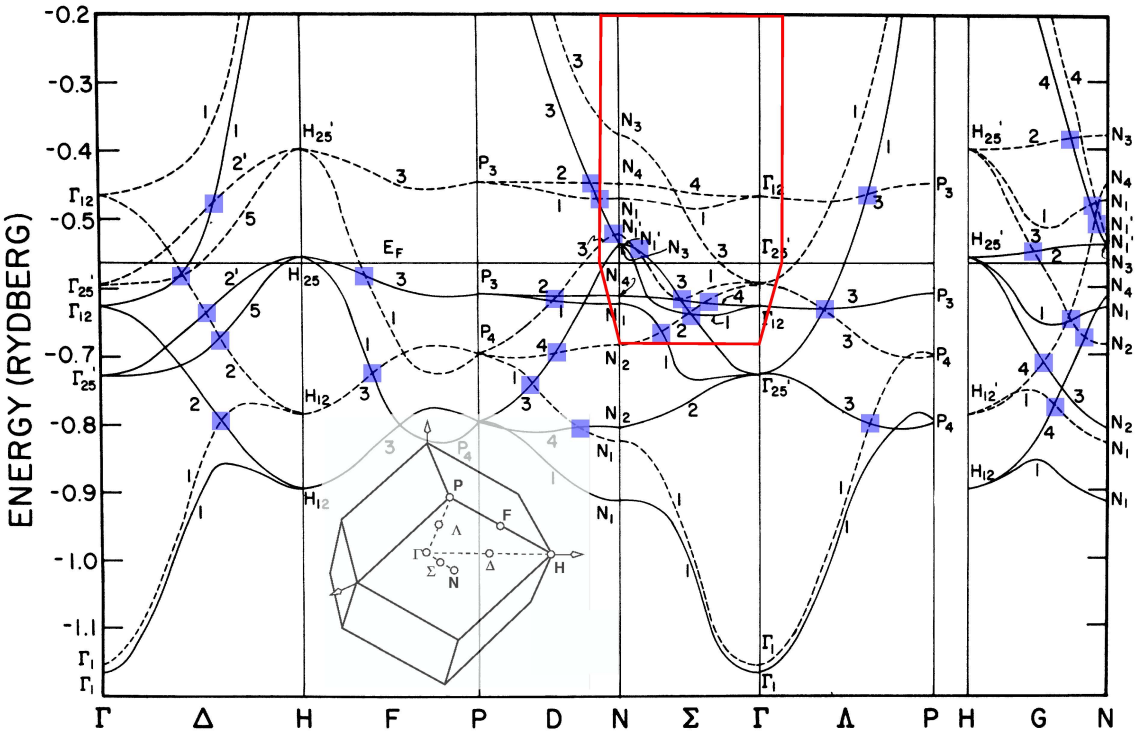

Figure 7.15 – Band structure of Fe: *Spin split energy bands of bcc Fe taken from [101]. The dashed lines represent minority spin bands, the solid lines majority spin bands. The measured area in k space is highlighted in red. The possible hybridization points are marked with blue squares.*

in our opinion partly excludes this explanation for the difference in τ_1 even if an optical contribution cannot be ruled out for times smaller than 50 fs.

Another explanation would be a difference in the response of spin and orbit. TR-MOKE and SHG are sensible to the orbital momentum whereas the s-pol measurements are only sensitive to the spin. But, like argued in Sec. 4.2, this can most probably be excluded.

But there is one more difference between both approaches: the probed area within the band structure. While MO measurements probe the whole k-space the s-pol measurements are limited to a narrow region of k values[†]. Fig 7.15 shows the band structure of iron. Only the red framed area is probed by our s-pol experiments. We believe, this is the major reason for the differences in the time constants. Calculations, which compare the resulting

[†]see Sec. 3.2

time constants of a wide spread measurement region with a narrow probing region within the k-space, sustain this explanation, as they show a slower response if the probing region is narrowed [102]. But further calculations have to be made to clarify the exact influence of a limited probing region on the resulting time constants.

In summary: With the above argumentation there remain two possible explanations for the s-pol results. Either the response of the spin and orbital momentum are different and the orbital response is much faster than the s-pol response while scaling equally in the amount of quenching. Or the difference in the probed region of the band structure leads to the different results. If this is the case the significance of the band structure was underestimated for a long time. In our opinion the results of this work point towards an explanation of ultrafast magnetization dynamics based on the Elliott Yafet spin flip mechanism together with a band structure containing hybridization points. Further experiments which probe different regions of the band structure can clarify this aspect.

Put together, the presented experiment could show, that it is possible to measure ultrafast magnetization dynamics with a direct access to the spin degree of freedom. The results fit well within the framework of the known data. The differences in the time constants of the different measurement strategies might point the way to an explanation of ultrafast magnetization dynamics and the underlying effects of the electron dynamics.

Appendix

A.1 Sample Preparation

We choose Tungsten as a substrate for two reasons: First, because it is easy to clean. That is, a few cycles of flashing and an Oxygen treatment yielded a clean surface with good crystalline structure. Second, the high free surface enthalpy of the (110) surface favours layer-by-layer growth, both for Iron and Cobalt [103].

Substrate Preparation

We grew iron and cobalt on a tungsten(110) single crystal. Therefore the W(110) crystal was treated with a well established standard procedure: First we degased the crystal at an elevated temperature of about 500°C until the pressure dropped to several 10^{-10} mbar. This was followed by an Oxygen-treatment. The chamber was filled with O_2 up to a pressure of 2×10^{-6} mbar and the crystal was heated up to $\approx$ 800°C for 20 min. After the pressure relaxed to low 10^{-10} mbar again, a series of rapid flashings of the crystal followed. That is, the crystal was rapidly heated up to 1800°C . Usually it took about three cycles of flashing to achieve a good pressure immediately afterwards. The crystal, prepared in this way, always showed an excellent LEED picture and the Auger-spectra usually showed only little carbon or oxygen (see Fig A.1).

The freshly prepared W-crystal was transfered to the MBE-chamber where the growth

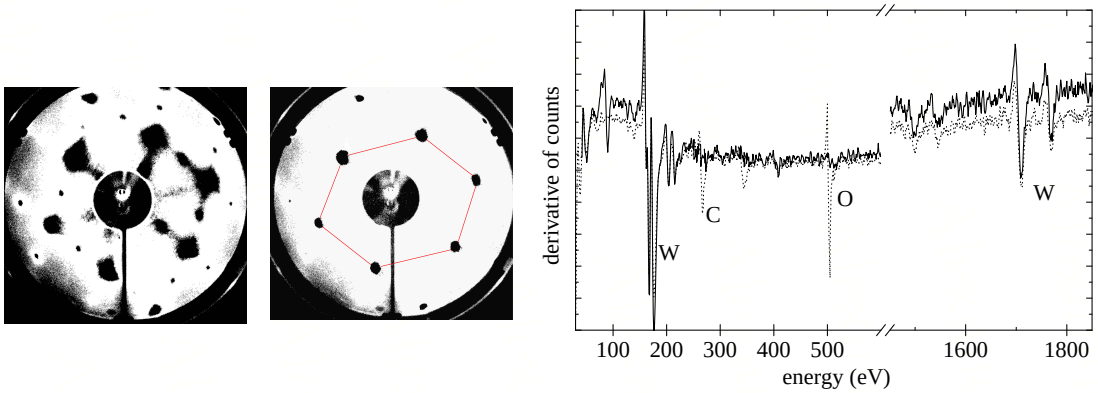

Figure A.1 – LEED and AES of W(110) *On the left you see two LEED pictures, the left was taken after one Oxygen-flashing cycle, the right after two more flashing procedures. On the right the corresponding Auger spectra are shown.*

took place. We evaporated Fe and Co out of tungsten crucibles by e-beam heating.* The pressure during evaporation always stayed within the 10^{-10} mbar range, usually it was around 4×10^{-10} mbar and the evaporation rate was kept around 0.2 ML min^{-1} , which was monitored with the QMB. The quality of the films was checked with AES and LEED.

Iron on Tungsten - Fe/W(110)

Fe grown on W(110) starts with a stable monolayer when grown between 300 and 900 K. This is followed by a layer-by-layer growth for the next 10 ML when grown at 300 to 500 K. The misfit between Fe an W is -9.4 %. It is not observable any more after around 10 ML. The anisotropy, putting the easy axis along the [1$\bar{1}$0] direction, originates from this misfit. A low coercive field ($H_c \approx$ 30 Oe for films around 10 ML thickness) indicates a good crystalline growth with a low density of defects [104].

We grew 8 ML Fe on W(110) at room temperature (RT) at a growth rate of 0.2 ML/min. With 8 ML there is still a well pronounced uniaxial anisotropy but the film can already be treated as bulk, which can be seen from thickness dependent DOS studies [105]. Moreover, with 8 ML the film is optically thin, that is, light penetrates the whole film. The prepared

*The usual alloying of the Fe or Co with W could not be observed, as was checked with AES with films grown on GaAs

iron films showed square hysteresis loops with a coercive field around 10 to 15 Oe with the easy axis lying along the W[1$\bar{1}$0] axis. The AES showed almost no Oxygen or Carbon, the LEED showed sharp peaks with no background.

Cobalt on Tungsten - Co/W(110)

The Co growth on W(110) starts as a pseudomorphic monolayer and makes a transition to close-packed in Nishiyama-Wassermann-orientation before the first ML is completed [103]. Above one monolayer Co growth at RT in a layer-by-layer fashion in a hcp-structure with a (0001)-surface. This is confirmed up to 12 ML. The Co [11$\bar{2}$0] direction is oriented parallel to the W[001] axis. Due to the lattice mismatch about five Co lattice spacings correspond to four W lattice spacings. This compresses the Co lattice about 1 % in the W[001] direction. This plus the shape anisotropy in a thin film puts the magnetic easy axis along the [1$\bar{1}$00]Co‖W[1$\bar{1}$0] direction [106, 107]. Above 4 ML Co already exhibits bulk like behavior [108]. The samples, grown at RT, showed square hysteresis loops with a coercive field of 40 Oe.

Iron on Galliumarsenide - Fe/GaAs(001)

As Fe/GaAs was used for most of the preliminary adjustment during the period of bringing the Mott-detector to operation it shall briefly be described. We used epi-ready, highly p-doped[†] GaAs wavers as substrate. The 2 inch wavers were cut into 5 by 5 mm pieces. The reverse side of the pieces was checked with a microscope for its etch-structure, as this indicates the easy axis of the Fe film to be grown. Without any further cleaning the pieces were put into the chamber. The GaAs was degased at 450°C until the pressure relaxed to its initial value. This was followed by Ar^+-ion sputtering at room temperature for half an hour with 1 kV electron energy followed by several hours with 0.5 kV until the AES showed no contamination. The surface was healed at an elevated temperature smaller than but close to 600°C until the LEED showed a clear reconstruction. The Fe-

[†]this ensured a good conductivity which was needed to prevent any space charge during the PE

evaporation was carried out like described above. The Fe/GaAs films showed nice square hysteresis loops with coercive fields as small as 5 Oe.

A.2 Pump-Probe Technique

In order to achieve a time resolution of the order of the pulse length of a modern laser, a special technique is applied, the so called stroboscopic pump-probe technique. For this the initial laser beam[‡] is split with a beam splitter. The two separated beams contain pulses, which will each reach the sample at the same time, if the separated beam paths are equal in length. Thus, if the length of one beam path can be adjusted with the aid of a translation stage, the delay time between the arrival of the two pulses can be set. Usually such a translation stage is passed to and fro. In this case a step width of the stage of 1 µm corresponds to a temporal resolution of $\approx$ 6 fs.[§] As the probe pulse responds to the state of the system at a certain time after the pump pulse the technique is called stroboscopic. To get a satisfying signal to noise ratio (SNR) a lot of experiments ($\approx 10^6$) are carried out with the stage set to the same position. An integration or summation over all experiments with the same delay will give the state of the system at the chosen delay time. A more detailed description of the pump-probe technique applied for TR-MOKE can be found in [109].

[‡]we consider a pulsed operation mode of the laser

[§]in our case the temporal resolution is limited by the pulse length as it is considerably longer than the time corresponding to the step width of the stage

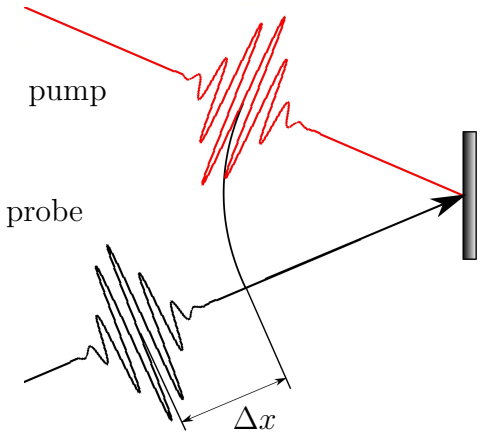

Figure A.2 – Schematic sketch of the pump-probe delay: *The probe pulse travels a longer distance Δx and thus arrives $\Delta x/c$ delayed compared to the pump beam.*

A.3 Maximum Angular Momentum Transfer by Photons

The estimation of the maximum angular momentum, that can be transferred from the photons of the pump pulse to the electronic system is straight forward. To determine whether this could lead to the measured signal, the amount of angular momentum that changes during the experiment, needs to be evaluated as well.

For the calculation we assume a pump pulse of $P_{\mathrm{dc}} = 30$ mW dc power, focused on a diameter of 50 µm (FWHM), with photons of energy $h\nu = 1.5$ eV. This corresponds to a fluence of $\rho_f = \frac{E_{\mathrm{P}}}{2A} = 10\ \mathrm{mJ\,cm^{-2}}$, with E_{P} being the energy per pulse ($E_{\mathrm{P}} = \frac{P_{\mathrm{dc}}}{\nu_{\mathrm{rep}}}$, repetition rate $\nu_{\mathrm{rep}} = 76$ kHz) and A the illuminated area. The factor of $1/2$ arises, as A is determined with the diameter of the beam at FWHM, which contains just half of its energy. We have to consider this factor as well, when calculating the number of photons within the area of the FWHM: $n_{\mathrm{FWHM}} = 1/2 \cdot n_{\mathrm{beam}}$. We can now calculate the maximum angular momentum of the photons:

$$L_{h\nu} = \frac{1}{2} n_{\mathrm{beam}} \hbar = \frac{1}{2} \frac{E_{\mathrm{P}}}{h\nu} \hbar = \frac{1}{2} \frac{P_{\mathrm{dc}}}{\nu_{\mathrm{rep}} h\nu} \hbar = 0.8 \cdot 10^{12} \hbar. \tag{A.2}$$

This pump pulse illuminates 8 ML of Fe. The molar volume of iron is $V_m = 7.09 \cdot 10^{-6}\ \mathrm{m^3/mol}$. So a disk of 50 µm diameter and 8 ML thickness contains

$$n_{\mathrm{Fe}} = \frac{V_{\mathrm{disc}}}{V_{\mathrm{atom}}} = \frac{8 V_{\mathrm{atom}}^{\frac{1}{3}} A}{V_{\mathrm{atom}}} = 8A \frac{V_m}{N_{\mathrm{A}}}^{-\frac{2}{3}} = 0.3 \cdot 10^{12} \tag{A.3}$$

Fe atoms. For each atom we can assume 2.2 $\hbar$ of angular momentum which is quenched by 30%. Thus the angular momentum changes by 0.66 $\hbar$ per atom or in total by

$$\Delta L_{\mathrm{Fe}} = n_{\mathrm{Fe}} \cdot 0.66 \cdot \hbar = 0.2 \cdot 10^{12} \hbar. \tag{A.4}$$

On a first glance the photons bring four times the angular momentum needed for the change. But, as linear polarized light is used, only half of them could transfer momentum with the right sign. Moreover it can be assumed, that maximum 20% are absorbed. This reduces the photon angular momentum by a factor of 0.1. With this maximum 40 % of the quenching could be reasoned by the angular momentum transfer from photons.

A.4 Limitations of the Experimental Resolution

This section aims to reassure, that with a given pulselength a physical process of comparable duration can indeed be resolved. The measurement of any physical process, $f(t)$, with a probe pulse, $g(t)$, of certain duration, τ (FWHM), yields a signal, which is a convolution of the two functions $f(t) * g(t)$. The convolution is defined as [110]:

$$[f * g](t) \equiv \frac{1}{\sqrt{2\pi}} \int_{-\infty}^{\infty} g(x) f(t-x) \mathrm{d}x. \tag{A.5}$$

To apply this to an experiment we choose

$$g(t) = \frac{1}{2\sqrt{\pi}\delta} \cdot e^{-\frac{t^2}{4\delta^2}}. \tag{A.6}$$

to represent the probe pulse as a Gaussian. δ is related to the FWHM, τ, by

$$\delta = \frac{\tau}{4\sqrt{\ln 2}}. \tag{A.7}$$

The physical process to be measured will be represented by a simple step function defined as a Boltzmann function:

$$f(t) = 1 - \frac{1}{1 + e^{\frac{t}{w}}}, \tag{A.8}$$

The Gaussian of Eqn. (A.6) is characterized by its FWHM, τ. The step function of Eqn. (A.8) is defined by its width w, at which the step reached 0.731 of its maximum.

The convolution $[f * g](t)$ relates to the function measured in the experiments. It is again a step function with a width, m, which is defined in analogy to w. It will contingently be broadened by the Gaussian. In Fig. A.3 the resulting function is plotted together with the Gaussian and the initial step function for different pulse durations. It is clearly visible, that only for a pulse much longer than the step function the measured signal is significantly broadened. The dependence of the measured width of the step on the pulselength and the initial step width is shown in Fig. A.4. It is remarkable, that the measured width is never far above the real width except for a very large pulsewidth compared to the step. For example, if a step with width $w = 50$ fs is probed by a pulse with FWHM $\tau = 100$ fs the resulting width is just $m = 57$ fs, $\tau = 200$ fs results in $m = 74$ fs, and $\tau = 300$ fs results in $m = 95$ fs.

With this it is clear, that the duration of the probe pulse has by far less influence on the outcome of the measurement than the duration of the pump pulse. As the pump pulse triggers the whole dynamics, these cannot be faster than the pulse itself. Thus, the experiments are limited most of all by the duration of the pump pulse.

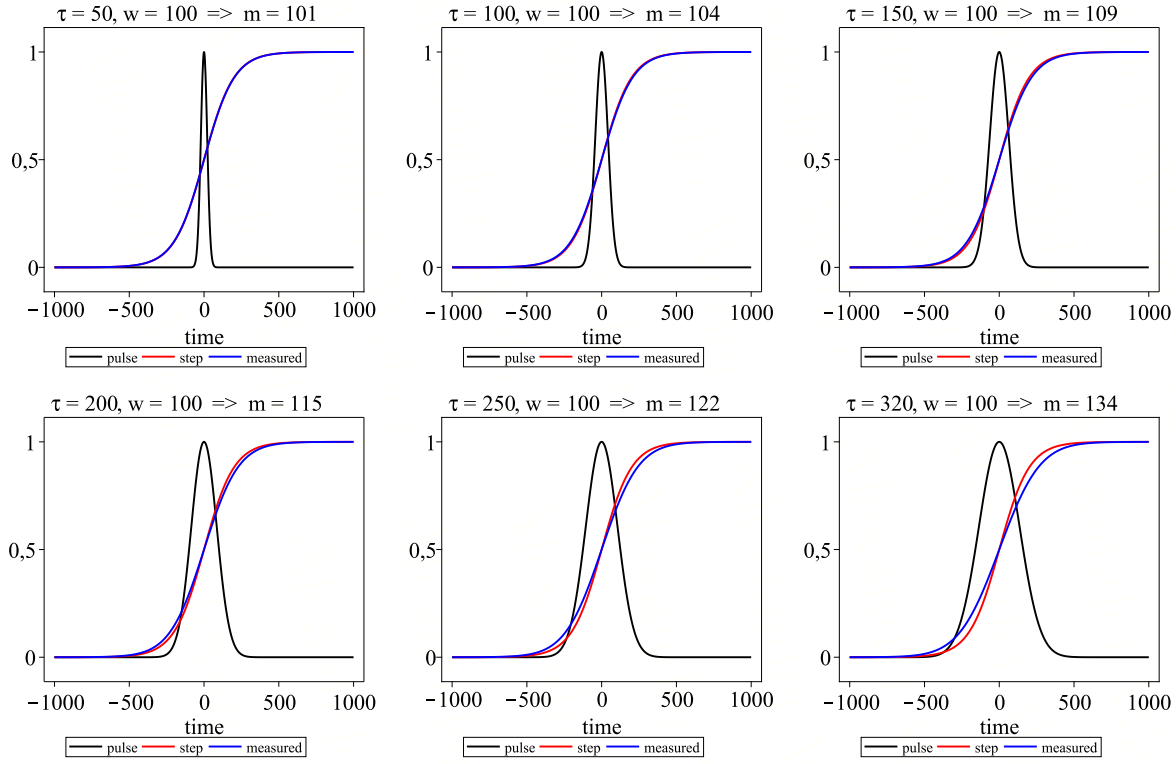

Figure A.3 – Convolution of a broadened step function with a Gaussian: *The plots shows the probe pulse as Gaussian with FWHM τ, a step function of width w, and the measured signal (m), for different values of the pulselength, τ. In the plot the Gaussian is scaled, so its maximum equals one. For the calculation it was normalized, so its area equaled one.*

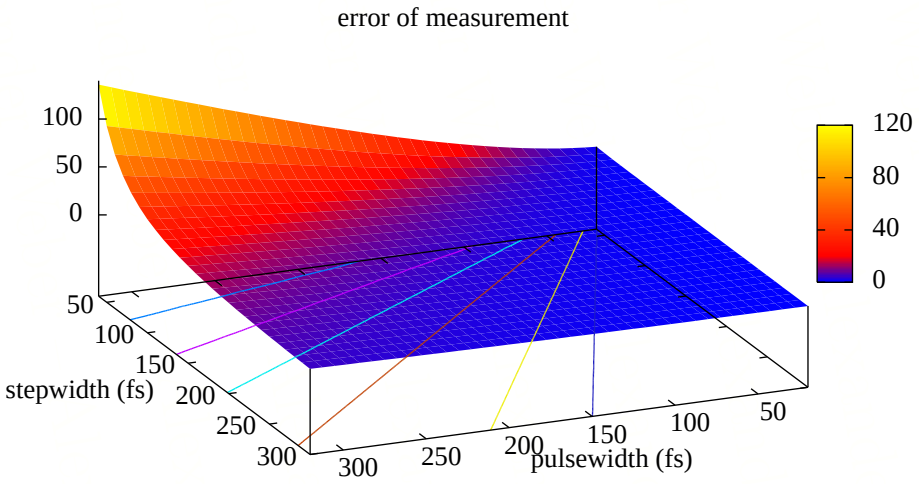

Figure A.4 – Relative error within the measured signal depending on the pulse duration and the width of the measured step function: *the z-axis gives the error of the measurement, $(m - w)/w$, in %. The lines on the base mark (from right to left) 1, 2, 5, 10, 20, and 50 % of deviation.*

A.5 Elliott-Yafet Spin-Flip Probability

In the following a short depiction of the application of the Elliott-Yafet spin-flip probability, α_{EY}, to ultrafast magnetization dynamics shall be given . For details the reader is referred to [85] and the references therein, mostly [81–83].

In a crystal with spin-orbit coupling an electronic state always consists of two contributions:

$$a_{\vec{k}}(\vec{r})e^{i\vec{k}\cdot\vec{r}} \quad |\uparrow\rangle \quad ; \quad \text{up-contribution, and} \tag{A.9}$$

$$a'_{\vec{k}}(\vec{r})e^{i\vec{k}\cdot\vec{r}} \quad |\downarrow\rangle \quad ; \quad \text{down-contribution.} \tag{A.10}$$

$\vec{k}$ is the wave vector of the electron. If $a > a'$ the crystal has a dominant spin-up contribution with a wave function given by:

$$\Psi_{\vec{k},\uparrow} = \left(a_{\vec{k}}(\vec{r})|\uparrow\rangle + a'_{\vec{k}}(\vec{r})|\downarrow\rangle\right) e^{i\vec{k}\cdot\vec{r}}. \tag{A.11}$$

A dominant spin-down state, $\Psi_{\vec{k},\downarrow}$ would have $a < a'$. In analogy to Fermi's golden rule, the transition from a spin-up state with the wave vector $\vec{k}$ to a spin-down state with the wave vector $\vec{k}+\vec{q}$ for a given phonon wave vector, $\vec{q}$, is represented by the matrix element

$$M_{(\vec{k}+\vec{q},\downarrow),(\vec{k},\uparrow)} = \langle \Psi_{\vec{k}+\vec{q},\downarrow} | w_{\vec{q}} | \Psi_{\vec{k},\uparrow} \rangle. \tag{A.12}$$

The number of electrons in dominant spin-up state is denoted as $n_\uparrow$, and the number of electrons in dominant spin-down states as $n_\downarrow$. The population difference is then $D = n_\uparrow - n_\downarrow$. If the number of transitions from spin-up to spin-down per unit time is depicted as $w_\searrow$, and $w_\nearrow$ the opposite transition, the time evolution of the population difference is

$$\frac{\mathrm{d}D}{\mathrm{d}t} = 2(w_\searrow - w_\nearrow). \tag{A.13}$$

The factor of 2 occurs, because one spin-flip changes the population difference by 2. This equation can be rewritten as

$$\frac{\mathrm{d}D}{\mathrm{d}t} = \frac{D_0 - D}{T_1}. \tag{A.14}$$

Here T_1 is the spin-relaxation time, which can be analytically derived from the matrix elements of Eq. A.12. Yafet gave an estimate for the matrix elements and showed, that

they scale with the minor contribution (a' for $a' < a$) of the wave function of a given state (Eq. A.11). Moreover, he could show, that for a system which is invariant with respect to time and space inversion, the spin-relaxation time is related to the relaxation time of the electrical resistivity by

$$\frac{1}{T} = pb^2 \frac{1}{\tau}. \tag{A.15}$$

This is the Elliott-Yafet relation. p is a material specific parameter between 1 and 10. The parameter b describes the degree of spin mixing of a given state and is usually defined as $0 \leq b^2 \leq 0.5$. Then $b^2 = 0$ stands for a pure spin state, either up ($a = 1$, $a' = 0$) or down ($a = 0$, $a' = 1$), $b^2 = 0.5$ resembles a totally mixed state. The product pb^2 is called the Elliott-Yafet spin-flip probability:

$$\alpha_{\mathrm{EY}} = pb^2. \tag{A.16}$$

This means, the higher the degree of spin-mixing of a given electron state, that is, the larger b^2, the larger will be α_{EY} and the higher is the probability for the spin to flip.

A.6 Glossary

Characters

symbol	description	dimension
A_i	asymmetry	
$C_{\mathrm{e,p,s}}$	electron, phonon, spin heat capacity	$\frac{\mathrm{J}}{\mathrm{kg}}$
$C_{\uparrow,\pm}$, $C_{\downarrow,\pm}$	electron count rates	s^{-1}
E	energy	1 eV = 1.602 10^{-19} J
E_0	energy of bottom of conduction band	eV
E_{F}	Fermi energy	13.6 eV=Ry
E_{kin}	kinetic energy	eV
$\vec{E}$	electric field	Vm^{-1}
$F^{(n)}$, $f^{(n)}$	Fresnel coefficient of nth order	
g_{ij}	coupling constant between heat baths	$\frac{\mathrm{J}}{\mathrm{kg\ s}}$
$\vec{G}$	crystal lattice vector	A^{-1}
H	magnetic field	Oe (1 Oe = $\frac{10^3}{4\pi} \cdot \frac{\mathrm{A}}{\mathrm{m}}$)
H_{c}	coercive field	Oe
$H(t)$	Heaveside step function	
h	Planck's constant (6.6261 10^{-34})	Js
$\hbar$	reduced Planck's constant ($\hbar = \frac{h}{2\pi} = 1.05510^{-34}$	Js
I	intensity	
$\vec{J}$	total angular momentum	Nms
K_{ij}	scattering probability	
k_{B}	Boltzmann's constant ($1.380658 \cdot 10^{-23}$)[111]	$\frac{\mathrm{J}}{\mathrm{K}}$
$\vec{L}_{\mathrm{e,p},h\nu}$	angular momentum of electron, phonon, photon	Nms, $\hbar$
$M = M(T)$	magnetization	G, (1 G = 10^{-4} T)
$\boldsymbol{M}$	magnetization vector	G
M_s	saturation magnetization	G
m	measured width until 0.731 of maximum is reached	
$m_{\mathrm{l,s}}$	quantum numbers for orbit and spin	

symbol	description	dimension
$\boldsymbol{m}$	normalized magnetization vector ($\boldsymbol{m} = \frac{\boldsymbol{M}}{M_s}$)	
m_i	components of the normalized magnetization vector	
$P = P(r,t)$	Energy deposited by the pump pulse	J
$\boldsymbol{P}$	Polarization	$\frac{\mathrm{C}}{\mathrm{m}^2}$
Q_v	magneto-optical coupling constant	$\frac{1}{\mathrm{G}}$
$S = S(\theta)$	Sherman function	
S_e	spin momentum	Nms, $\hbar$
T	temperature	K
T_C	Curie temperature	K
$T_\mathrm{e,p,s}$	temperature of electron, phonon, and spin baths	K
w	width until 0.731 of maximum is reached	
α	phenomenological damping constant	
α_EY	Elliott Yafet spin flip probability	
Δ	laser induced changes, crystal direction	
ε_0	dielectric permittivity constant ($8.8542 \cdot 10^{-12}$) [111]	$\frac{\mathrm{C}}{\mathrm{Vm}}$
$\hat{\boldsymbol{\varepsilon}}$	dielectric permittivity tensor ($\varepsilon_0 \hat{\boldsymbol{\varepsilon}}_\mathrm{r}$)	$\frac{\mathrm{C}}{\mathrm{Vm}}$
ε_K	Kerr ellipticity	
θ_K	Kerr rotation	$^\circ$
κ	thermal conductivity	$\frac{\mathrm{W}}{\mathrm{m\ K}}$
Λ	crystal direction	
λ	wavelength	nm
λ_e	electron mean free path	Å
μ_B	Bohr magneton ($\frac{e}{2m}\hbar = 9.274 \cdot 10^{-24}$) [112]	$\frac{\mathrm{Jm}}{\mathrm{Vs}}$
$\mu_\mathrm{e,s}$	magnetic moment of electron, spin	μ_B
ν	light frequency	Hz
ρ_f	fluence (flux density)	$\frac{\mathrm{mJ}}{\mathrm{cm}^2}$
Σ	crystal direction	
σ	optical penetration depth	Å
$\sigma(\theta,\phi)$	differential scattering cross section	
τ	FWHM of probe pulse	fs

symbol	description	dimension
$\tau_{1,2,3}$	characteristic times for spin dynamics	fs
τ_0	material specific constant for (e-e) scattering	s
τ_{ee}	(e-e) scattering time	s
τ_{th}	thermalization time	ps
Φ	work function	eV
χ	susceptibility ($\boldsymbol{\chi} = (\hat{\boldsymbol{\varepsilon}} - \hat{1})\varepsilon_0$)	$(\frac{\mathrm{C}}{\mathrm{Vm}})^2$

Abbreviations

	2PPE	2 Photon PhotoEmission
	2EF	2 Exponentials Fit
	3EF	3 Exponentials Fit
A		
	AES	Auger Electron Spectroscopy
B		
	BBO	Beta-Barium bOrate (β-BaB_2O_4)
D		
	DOS	Density Of States
E		
	e	Electron
F		
	FWHM	Full Width at Half Maximum
I		
	IGP	Ion Getter Pump
	IR	Infra Red
L		
	LEED	Low Energy Electron Diffraction
M		

MBE	Molecular Beam Epitaxy
ML	Mono Layer
MO	Magneto-Optic(al)
MOKE	Magneto-Optic Kerr Effect
MSHG	Magnetization-induced Second Harmonic Generation

P

p	Phonon
PE	PhotoEmission
PIPS	Particle ImPlanted Silicon diode

Q

QMB	Quarz Micro Balance

S

s	Spin
s-pol	Spin-POLarization
SHG	Second Harmonic Generation
SNR	Signal to Noise Ratio
SOC	Spin Orbit Coupling

T

TR-MOKE	Time-Resolved Magneto-Optical Kerr Effect

U

UHV	Ultra High Vacuum
UV	Ultra Violett

X

XMCD	X-ray Magnetic Circular Dichroism

List of Figures

List of Tables

Bibliography

[1] J. Kerr. A New Relation between Electricity and Light. *Philosophical Magazine*, 3(321), 1877.

[2] H. Le Gall, R. Sbiaa, and S. Pogossian. Present and future of magnetooptical recording materials and technology. *Journal of Alloys and Compounds*, 275-277:677–684, 1998.

[3] P. Bruno. Die Entdeckung des Riesen-Magnetowiderstandes. *Physik in unserer Zeit*, 38(6):272–273, 2007.

[4] J. F. Gregg. Spintronics, A growing science. *Nature Materials*, 6:798–799, 2007.

[5] J-U. Thiele, S. Maat, and E. E. Fullerton. FeRh/FePt exchange spring films for thermally assisted magnetic recording media. *Applied Physics Letters*, 82(17):2859–2861, 2003.

[6] M. Albrecht, J-U. Thiele, and A. Moser. Terabit-Speicher - bald Realität oder nur Fiktion? *Physik Journal*, 2(10):25–31, 2003.

[7] B. Koopmans, M. van Kampen, J. T. Kohlhepp, and W. J. M. de Jonge. Ultrafast Magneto-Optics in Nickel: Magnetism or Optics? *Physical Review Letters*, 85(4):844–847, 2000.

[8] A. Scholl, L. Baumgarten, R. Jacquemin, and W. Eberhardt. Ultrafast Spin Dynamics of Ferromagnetic Thin Films Observed by fs Spin-resolved Two-Photon Photoemission. *Physical Review Letters*, 79(25):5146–5149, 1997.

[9] J. Hohlfeld, E. Matthias, R. Knorren, and K.H. Bennemann. Nonequilibrium Magnetization Dynamics of Nickel. *Physcal Review Letters*, 78(25):4861–4864, 1997.

[10] S. I. Anisimov, B. L.Kapeliovich, and T. L. Perel'man. Electron emission from metal surfaces exposed to ultrashort laser pulses. *Soviet Physics-JETP*, 39:375–377, 1974.

[11] E. Beaurepaire, J.-C. Merle, A. Daunois, and J.-Y. Bigot. Ultrafast Spin Dynamics in Ferromagnetic Nickel. *Physical Review Letters*, 76(22):4250–4253, 1996.

[12] W. Hübner and G. P. Zhang. Ultrafast spin dynamics in nickel. *Physical Review B*, 58(10):R5920–5923, 1998.

[13] N. Kazantseva, U. Nowak, R. W. Chantrell, J. Hohlfeld, and A. Rebei. Slow recovery of the magnetisation after a sub-picosecond heat pulse. *Europhysics Letters*, 81:27004, 2008.

[14] H.-S. Rhie, H. A. Dürr, and W. Eberhardt. Femtosecond Electron and Spin Dynamics in Ni/W(110) films. *Physical Review Letters*, 90(24):247201, 2003.

[15] Luca Guidoni, Eric Beaurepaire, and Jean-Yves Bigot. Magneto-optics in the ultrafast regime: Thermalization of spin populations in ferromagnetic films. *Phys. Rev. Lett.*, 89(1):017401, 2002.

[16] J. Kerr. On the Magnetism of Light and the Illumination of Magnetic Lines of Force. *Report of the British Association for the Advancement of Science*, S5(85), 1876.

[17] P. N. Argyres. Theory of the Faraday and Kerr Effect in Ferromagnetics. *Physical Review*, 97(2):334–345, 1955.

[18] S. D. Bader. SMOKE. *Journal of Magnetism and Magnetic Materials*, 100:440–454, 1991.

[19] E. Jäger and R. Perthel. *Magnetische Eigenschaften von Festkörpern.* Akademie Verlag, 2nd edition, 1996.

[20] A. Hubert and R. Schäfer. *Magnetic Domains - The Analysis of Magnetic Microstructures.* Springer, 1998.

[21] N. N. Dadoenkova, T. Andersen, and W. Hübner. Nonlinear surface magneto-optics of ferromagnetic Ni/Cu(001) from first principles. *Applied Physics B*, 74:705–709, 2002.

[22] O. Eriksson, B. Johansson, R. C. Albers, and A. M. Boring. Orbital magnetism in Fe, Co, and Ni. *Physikal Review B*, 42(4):2704–2710, 1990.

[23] Djordjevic M., Lüttich M., Moschkau P., Guderian p., Kampfrath T., Ulbrich R. G., Münzenberg M., Flesch W., and Moodera J. S. Comprehensive view on ultrafast dynamics of ferromagnetic films. *physica status solidi*, 3(5):1347–1358, 2006.

[24] H. Regensburger, R. Vollmer, and J. Kirschner. Time-resolved magnetization-induced second-harmonic generation from the Ni(110) surface. *Phys. Rev. B*, 61(21):14716–14722, 2000.

[25] T. Kampfrath, R. G. Ulbrich, F. Leuenberger, M. Münzenberger, B. Sass, and W. Felsch. Ultrafast magneto-optical response of iron thin films. *Physical Review B*, 65(104429), 2002.

[26] B. Koopmans, M. van Kampen, and W. J. M. de Jonge. Experimental access to femtosecond spin dynamics. *Journal of Physics Condensed Matter*, 2003.

[27] G. P. Zhang, W. Hübner, G. Lefkidis, Y. Bai, and T. F. George. Paradigm of the time-resolved magneto-optical kerr effect for femtosecond magnetism. *Nature physics*, 5:499–502, 2009.

[28] N. Richard, A. Dereux, E. Bourillot, T. David, J. P. Goudonnet, F. Scheurer, and E. Beaurepaire. Kerr and Faraday Rotations of Magneto-Optical Multilayers under the Condition of Total Internal Reflection. *Physica Status Solidi A*, 215:225–232, 1999.

[29] J. Hohlfeld. *Ultrafast Electron-, Lattice- and Spin-Dynamics in Metals - Investigated by Linear and Nonlinear Optical Techniques.* PhD thesis, Freie Universität Berlin, 1998.

[30] J. E. Sipe, D. J. Moss, and H. M. van Driel. Phenomenological theory of optical

second- and third-harmonic generation from cubic centrosymmetric crystals. *Phys. Rev. B*, 35(3):1129–1141, 1987.

[31] J. Stöhr. X-ray magnetic circular dicroism spectroscopy of transition metal thin films. *Journal of Electron Spectroscopy*, 75:253–272, 1995.

[32] Stamm C., Kachel T., Pontius N., Mitzner R., Quast T., Holldack K., Khan S. Lupulescu C., Aziz E. F., Wietstruk M., Dürr H. A., and Eberhardt W. Femtosecond modification of electron localization and transfer of angular momentum in nickel. *Nature materials*, 6:740–743, 2007.

[33] K. Carva, D. Legut, and P. M. Oppeneer. Influence of laser-excited electron distributions on the X-ray magnetic circular dichroism spectra: Implications for femtosecond demagnetization in Ni. *EPL (Europhysics Letters)*, 86(5):57002, 2009.

[34] C. N. Berglund and W. E. Spicer. Photoemission studies of copper and silver: Theory. *Phys. Rev.*, 136(4A):A1030–A1044, 1964.

[35] Stefan Hüfner. *Photoelectron Spectroscopy*. Springer, 3 edition, 2003.

[36] J. Braun. The theory of angle-resolved ultraviolet photoemission and its applications to ordered materials. *Reports on Progress in Physics*, 59:1267–1338, 1996.

[37] C. N. Berglund and W. E. Spicer. Photoemission studies of copper and silver: Experiment. *Phys. Rev.*, 136(4A):A1044–A1064, 1964.

[38] W. H. Rippard and R. A. Buhrman. Spin-Dependent Hot Electron Transport in Co/Cu Thin Films. *Physical Review Letters*, 84(5):971–974, 2000.

[39] T. Banerjee, J. C. Lodder, and R. Jansen. Origin of the spin-asymmetry of hot-electron transmission in Fe. *Physical Review B*, 76(140407), 2007.

[40] Bruce A. Gurney, Virgil S. Speriosu, Jean-Pierre Nozieres, Harry Lefakis, Dennis R. Wilhoit, and Omar U. Need. Direct measurement of spin-dependent conduction-electron mean free paths in ferromagnetic metals. *Physical Review Letters*, 71(24):4023, 1993.

[41] Henri-Jean Drouhin. Low-energy electron mean free path and its spin dependence in transition metals. *Physical Review B*, 56(23):14886, 1997.

[42] E. Heindl. private communication, 2009.

[43] H. B. Michaelson. The work function of the elements and its periodicity. *Journal of Applied Physics*, 48(11):4729–4733, 1977.

[44] N. F. Mott. The Scattering of Fast Electrons by Atomic Nuclei. *Proceedings of the Royal Society of London, A*, 124(794):425–442, 1929.

[45] P. A. M. Dirac. The Quantum Theory of the Electron. *Proceedings of the Royal Society of London, A*, 117(778):610–624, 1929.

[46] N. F. Mott and H. S. W. Massey. *The Theory of Atomic Collisions*, chapter IX. Clarendon Press, Oxford, 3 edition, 1971.

[47] J. Kessler. *Polarized Electrons*. Springer, Berlin, 2. ed. edition, 1985.

[48] N. Sherman. Coulomb Scattering of Relativistic Electrons by Point Nuclei. *Physical Review*, 103(6):1601–1607, 1956.

[49] Teruo Kohashi, Makoto Konoto, and Kazuyuki Koike. Systematic Experiment of Mott Scattering. *Japanese Journal of Applied Physics*, 45(8A):6468–6474, 2006.

[50] J. Güdde, U. Conrad, V. Jähnke, J. Hohlfeld, and E. Matthias. Magnetization dynamics of Ni and Co films on Cu(001) and of bulk nickel surfaces. *Physical Review B*, 59(10):R6608–R6611, 1999.

[51] U. Conrad, J. Güdde, V. Jähnke, and E. Matthias. Ultrafast electron and magnetization dynamics of thin Ni and Co films on Cu(001) observed by time-resolved SHG. *Applied Physics B*, 68:511–517, 1999.

[52] Ganping Ju, A. Vertikov, A. V. Nurmikko, C. Canady. Gang Xiao, R.F.C. Farrow, and A. Cebolada. Ultrafast nonequilibrium spin dynamics in a ferromagnetic thin film. *Physical Review B*, 57(2):R700–R703, 1998.

[53] E. Beaurepaire, M. Maret, V. Halté, J.-C. Merle, A. Daunois, and J.-Y.Bigot. Spin

dinnamics in $CoPt_3$ alloy films: A magnetic phase transition in the femtosecond time scale. *Physical Review B*, 58(18):12134 – 12137, 1998.

[54] L. Guidoni, E. Beaurepaire, and J.-Y. Bigot. Magneto-optics in the ultrafast regime: Thermalization of spin populations in ferromagnetic films. *Physical Review Letters*, 89(1):017401, 2002.

[55] B. Koopmans, M. van Kampen, J. T. Kohlhepp, and W. J. M. de Jonge. Femtosecond spin dynamics of epitaxial Cu(111)/Ni/Cu wedges. *Journal of Applied Physics*, 87(9):5070–5072, 2000.

[56] G. P. Zhang and W. Hübner. Femtosecond spin dynamics in the time domain. *Journal of Applied Physics*, 85(8):5657–5659, 1999.

[57] G. P. Zhang and W. Hübner. Femtosecond electron and spin dynamics probed by nonlinear optics. *Journal of Applied Physics B*, 68:495–499, 1999.

[58] G. P. Zhang and W. Hübner. Laser-induced Ultrafast Demagnetization in Ferromagnetic Metals. *Physical Review Letters*, 85(14):3025–3028, 2000.

[59] B. Koopmans, G. Malinowski, F. Dalla Longa, D. Steiauf, M. Fähnle, T. Roth, M. Cinchetti, and M. Aeschlimann. Explaining the paradoxical diversity of ultrafast laser-induced demagnetization. *Nature Materials*, 9:259–265, 2010.

[60] T. Ogasawara, K. Ohgushi, Y. Tomioka, K. S. Takahashi, H. Okamoto, M. Kawasaki, and Y. Tokura. General Features of Photoinduced Spin Dynamics in Ferromagnetic and Ferrimagnetic Compounds. *Physical Review Letters*, 94(087202), 2005.

[61] M. van Kampen, J. T. Kohlhepp, W. J. M. de Jonge, B. Koopmans, and R. Coehoorn. Sub-picosecond electron and phonon dynamics in nickel. *Journal of Physics Condensed Matter*, 17:6823–6834, 2005.

[62] Rogier H. M. Groeneveld, Rudolf Sprik, and Ad Lagendijk. Femtosecond spectroscopy of electron-electron and electron-phonon energy relaxation in Ag and Au. *Phys. Rev. B*, 51(17):11433–11445, 1995.

[63] F. Dalla Longa, J. T. Kohlhepp, W. J. M. de Jonge, and B. Koopmans. Influence of photon angular momentum on ultrafast demagnetization in nickel. *Physical Review Letters*, 75(22):224431, 2007.

[64] R. Wilkis, R. J. Hicken, M. Ali, B. J. Hickey, J. D. R. Buchanan, A. T. G. Pym, and B. K. Tanner. Investigation of ultrafast demagnetization and cubic optical nonlinearity of Ni in the polar geometry. *Journal of Applied Physics*, 95(11):7441, 2004.

[65] A. V. Kimel, A. Kirilyuk, A. Tsvetkov, R. V. Pisarev, and Th. Rasing. Laser-induced ultrafast spin reorientation in the antiferromagnet $TmFeO_3$. *Nature*, 429:850, 2004.

[66] F. Hansteen, A. V. Kimel, A. Kirilyuk, and Th. Rasing. Femtosecond Photomagnetic Switching of Spins in Ferrimagnetic Garnet Films. *Physical Review Letters*, 95:047402, 2005.

[67] C. D. Stanciu, F. Hansteen, A. V. Kimel, A. Tsukamoto, A. Itoh, A. Kirilyuk, and Th. Rasing. Ultrafast Interaction of the Angular Momentum of Photons with Spins in the Metallic Amorphous Alloy GdFeCo. *Physical Review Letters*, 98:207401, 2007.

[68] E. Beaurepaire, G. M. Turner, S. M. Harrel, M. C. Beard, J.-Y. Bigot, and C. A. Schuttenmaer. Coherent teraherz emission from ferromagnetic films excited by femtosecond laser pulses. *Applied Physics Letters*, 84(18):3465–3467, 2004.

[69] J.-Y. Bigot, M. Vomir, and E. Beaurepaire. Coherent ultrafast magnetism induced by femtosecond laser pulses. *Nature Physics*, 5:515–520, 2009.

[70] DPG-Frühjahrstagung Dresden. *Femtosecond Dynamics of Spin and Orbital Angular Momentum in Nickel*, number MA 35.2. C. Stamm and N. Pontius and K. Holldack and T. Quast and T. Kachel and M. Wietstruk and R. Mitzner and H. A. Dürr, 2009.

[71] C. Stamm, N. Pontius, T. Kachel, M. Wietstruk, and H. A. Dürr. Femtosecond x-ray absorption spectroscopy of spin and orbital angular momentum in photoexcited Ni films during ultrafast demagnetization. *Phys. Rev. B*, 81(10):104425, 2010.

[72] C. Boeglin, E. Beaurepaire, V. Halte, V. Lopez-Flores, C. Stamm, N. Pontius, H. A. Dürr, and J.-Y. Bigot. Distinguishing the ultrafast dynamics of spin and orbital moments in solids. *Nature*, 465:458–461, 2010.

[73] M. Binder. *Magnetization Dynamics of Rare-Earth Doped Magnetic Films*. PhD thesis, Universität Regensburg, 2006.

[74] B. Koopmans, J. J. M. Ruigrok, F. Dalla Longa, and W. J. M. de Jonge. Unifying Ultrafast Magnetization Dynamics. *Physical Review Letters*, 95(26):267207, 2005.

[75] M. Binder, A. Weber, O. Mosendz, G. Wolterdorf, M. Izquierdo, I. Neudecker, J. R. Dahn, T. D. Hatchard, J.-U. Thiele, C. H. Back, and M. R. Scheinfein. Magnetization dynamics of the ferrimagnet CoGd near the compensation of magnetization and angular momentum. *Physical Review B*, 74:134404, 2006.

[76] J. Walowski, G. Müller, M. Djordjevic, M. Münzenberg, M. Kläui, C. A. F. Vaz, and J. A. C. Bland. Energy equilibration processes of electrons, magnons, and phonons at the femtosecond time scale. *Physical Review Letters*, 101(23):237401, 2008.

[77] I. Radu, G. Woltersdorf, M. Kiessling, A. Melnikov, U. Bovensiepen, J.-U. Thiele, and C. H. Back. Laser-Induced Magnetization Dynamics of Lanthanide-Doped Permalloy Thin Films. *Physical Review Letters*, 102:117201, 2009.

[78] W. Hübner and K. H. Bennemann. Simple theory for spin-lattice relaxation in metallic rare-earth ferromagnets. *Phys. Rev. B*, 53(6):3422–3427, 1996.

[79] A. Vaterlaus, T. Beutler, D. Guarisco, M. Lutz, and F. Meier. Spin-lattice relaxation in ferromagnets studied by time-resolved spin-polarized photoemission. *Physical Review B*, 46(9):5280–5286, 1992.

[80] B. Koopmans, H.H.J.E. Kicken, M. van Kampen, and W.J.M. de Jonge. Microscopic model for femtosecond magnetization dynamics. *Journal of Magnetism and Magnetic Materials*, 286:271 – 275, 2005. Proceedings of the 5th International Symposium on Metallic Multilayers.

[81] R. J. Elliott. Theory of the Effect of Spin-Orbit Coupling on Magnetic Resonance in Some Semiconductors. *Physical Review*, 96(2):266, 1954.

[82] Y. Yafet. Relaxation and resonance. *Journal of Applied Physics*, 42(4):1564, 1971.

[83] J. Fabian, A. Matos-Abiague, C. Ertler, P. Stano, and I. Žutić. *Acta Physica Slovaca*, volume 57. Slovak Academy of Sciences, 2007.

[84] M. Cinchetti, M. Sánchez Albaneda, D. Hoffmann, T. Roth, J.-P. Wüstenberg, M. Krauß, O. Andreyev, H. C. Schneider, M. Bauer, and M. Aeschlimann. Spin-Flip Processes and Ultrafast Magnetization Dynamics in Co: Unifying the Microscopic and Macroscopic View of Femtosecond Magnetism. *Physical Review Letters*, 97(17):177201, 2006.

[85] D. Steiauf and M. Fähnle. Elliott-Yafet mechanism and the discussion of femtosecond magnetization dynamics. *Physical Review B*, 79:140401, 2009.

[86] M. Pickel, A. B. Schmidt, F. Giesen, J. Braun, J. Minár, H. Ebert, M. Donath, and M. Weinelt. Spin-orbit hybridization points in the face-centered-cubic cobalt band structure. *Physical Review Letters*, 101(6):066402, 2008.

[87] P. Mavropoulos and N. Papanikolaou. *Computational Nanoscience: Do It Yourself!*, volume 31 of *NIC Series*, chapter The Korringa-Kohn-Rostoker (KKR) Green Function Method - I. Electronic Structure of Periodic Systems. Forschungszentrum Jülich, 2006.

[88] S. Förster, G. Baum, M. Müller, and H. Steidl. Oxygen adsorption on Fe/W(110) and Co/W(110) thin films: Surface magnetic properties. *Physical Review B*, 66:134427, 2002.

[89] V. N. Petrov, V. V. Grebenshikov, B. D. Grachev, and A. S. Kamochkin. New compact classical 40 kV mott polarimeter. *Review of Scientific Instruments*, 74(3):1278–1281, 2003.

[90] Coherent Laser Group, editor. *Operator's Manual RegA Model 9000 Laser*, chapter 8 Theory of Operation. Coherent Inc.

[91] M. Bauer, M. Wessendorf, D. Hoffmann, C. Wiemann, A. Mönnich, and M. Aeschlimann. Time-resolved 2PPE: Probing adsorbate motion on femtosecond time-scales

– what is the role of the laser bandwidth? *Applied Physics A: Materials Science & Processing*, 80:987–994, 2005.

[92] B. Heitkamp, F. Kronast, L. Heyne, H. A. Dürr, W. Eberhardt, S. Landis, and B. Rodmacq. Femtosecond spin dynamics of ferromagnetic thin films and nanodots probed by spin polarized photoemission electron microscopy. *Journal of Physics D Applied Physics*, 41(16):164002–+, 2008.

[93] Y.-L. He and G.-C. Wang. Observation of dynamic scaling of magnetic hysteresis in ultrathin ferromagnetic Fe/Au(001) films. *Physical Review Letters*, 70:2336–2339, 1993.

[94] M. Galaktionov. private communication.

[95] Y. B. Xu, D. Greig, E. A. Seddon, and J. A. D. Matthew. Spin-resolved photoemission of in situ sputtered iron and iron-yttrium alloys. *Physical Review B*, 55(17):11442 – 11447, 1997.

[96] A. Vaterlaus, D. Guarisco, M. Lutz, m. Aeschlimann, M. Stampanoni, and F. Meier. Different spin and lattice temperatures observed by spin-polarized photoemission with picosecond laser pulses. *Journal of Applied Physics*, 67(9):5661–5663, 1990.

[97] E. Carpene, E. Mancini, C. Dallera, M. Brenna, E. Puppin, and S. De Silvestri. Dynamics of electron-magnon interaction and ultrafast demagnetization in iron thin films. *Physical Review B*, 78:174422, 2008.

[98] M. Farle, A. Berghaus, Yi Li, and K. Baberschke. Hard-axis magnetization of ultrathin Ni(111) films on W(110): An experimental method to measure the magneto-optic Kerr effect in ultra high vacuum. *Phyical Review B*, 42(7):4873–4876, 1990.

[99] C. A. C. Bosco, A. Azevedo, and L. H. Aciolo. Substrate dependent ultrafast dynamics in thin NiFe films. *Applied Physics Letters*, 83(9):1767–1769, 2003.

[100] G.K.L. Marx, H. L. Elmers, and G. Schönhense. Magneto-optical Linear Dichroism in Threshold Photoemission Electron Microscopy of polycrystalline Fe Films. *Physical Review Letters*, 84(25):5888–5891, 2000.

[101] J. Callaway and C. S. Wang. Energy bands in ferromagnetic iron. *Physical Review B*, 16(5):2095–2105, 1977.

[102] M. Aeschlimann T. Roth, S. Allenbrand. private communication, 2009.

[103] M. Pratzer, H. J. Elmers, and M. Getzlaff. Heteroepitaxial growth of Co on W(110) investigated by scanning tunneling microscopy. *Physicl Review B*, 67:153405, 2003.

[104] H. J. Elmers and U. Gradmann. Magnetic Anisotropies in Fe(110) Films on W(110). *Applied Physics A*, 51:255–263, 1990.

[105] S. Stankov, R. Röhlsberger, T. Ślezak, M. Sladecek, B. Sepiol, G. Vogl, A. I. Chumakov, R. Rüffer, N. Spiridis, J. Łażewski, K. Parliński, and J. Korecki. Phonons in iron: From the Bulk to an Epitaxial Monolayer. *Physical Review Letters*, 99(18):185501, 2007.

[106] M. Etzkorn, P. S. Anil Kumar, W. Tang, Y. Zhang, and J. Kirschner. High-wave-vector spin waves in ultrathin Co films on W(110). *Physical Review B*, 72:184420, 2005.

[107] H. Fritzsche, J. Kohlhepp, and U. Grandmann. Epitaxial strain and magnetic anisotropy in ultrathin Co films an W(110). *Physical Review B*, 22(51):15933–15941, 1995.

[108] H. Knoppe and E. Bauer. Electronic structure of ultrathin cobalt films on W(110). *Physical Review B*, 48(3):1794–1805, 1993.

[109] A. Weber. Ultrafast Magnetization Dynamics induced by Femtosecond Laser Pulses. Diplomarbeit, Universität Regensburg, 2004.

[110] G. B. Arfken and H. J. Weber. *Mathematical Methods for Physicists*. Academic Press, London, Orlando, San Diego, Burlington, 5th edition, 2001.

[111] H. Kuchling. *Taschenbuch der Physik*. Fachbuchverlag Leipzig, 15 edition, 1995.

[112] C. Gerthsen and H. Vogel. *Physik*. Springer, Berlin, 17 edition, 1993.

Acknowledgments

Finally I want to thank all thous, who mainly contributed to the success of the project during the last five years.

- First, I am grateful to my supervisor, Prof. C.H. Back, for giving me the opportunity to work on such an ambitious project. I really enjoyed the work in the lab even though there were hard times with hardly any hope on success.
- Special thanks to Thobias Söckl for his support on all the complicated constructions related to the measurement and evaporation chamber. Also I would like to thank Dieter Schierl for his constantly immediate support if anything was needed.
- I also would like to thank Sabine Allenbrand, Thobis Roth, and Daniel Steil for sharing their knowledge on the calculation of electron dynamics, and the lively discussions on the topic.
- I am thankful to Emanuel Heindl and Frank Hoffmann. They always found time to discuss problems and to contemplate on possible solutions.
- Many thanks to Christian Meurer, Christian Chwala, and Andrea Eschenlohr for the pleasant time we spent together in the lab.
- Special thanks to Michael Binder, my supervisor during my diploma thesis, for introducing me to the field of ultrafast magnetization dynamics and teaching me the art of vacuum techniques.
- Many thanks to Julien Vigroux for the faithful company, the inspiring discussions, and the great time in the office.
- And I would like to thank the whole institute for the nice atmosphere and the pleasant time.

Finally, many thanks to my parents for their constant support during my studies and my work, which alone made this path possible for me. And, of course, to Johanna, for her great patience during the times I had to cut our joint time short in favor of the measurements and for her great moral support.